

Removal of arsenic and metals from groundwater impacted by mine waste using zero-valent iron and organic carbon: Laboratory column experiments

Angai, J. U., Ptacek, C. J., Pakostova, E., Bain, J. G., Verbuyst, B. R. & Blowes, D. W.

Author post-print (accepted) deposited by Coventry University's Repository

Original citation & hyperlink:

Angai, JU, Ptacek, CJ, Pakostova, E, Bain, JG, Verbuyst, BR & Blowes, DW 2022, 'Removal of arsenic and metals from groundwater impacted by mine waste using zero-valent iron and organic carbon: Laboratory column experiments', *Journal of Hazardous Materials*, vol. 424, no. Part A, 127295.

<https://dx.doi.org/10.1016/j.jhazmat.2021.127295>

DOI 10.1016/j.jhazmat.2021.127295

ISSN 0304-3894

ESSN 1873-3336

Publisher: Elsevier

© 2021, Elsevier. Licensed under the Creative Commons Attribution-NonCommercial-NoDerivatives 4.0 International <http://creativecommons.org/licenses/by-nc-nd/4.0/>

Copyright © and Moral Rights are retained by the author(s) and/ or other copyright owners. A copy can be downloaded for personal non-commercial research or study, without prior permission or charge. This item cannot be reproduced or quoted extensively from without first obtaining permission in writing from the copyright holder(s). The content must not be changed in any way or sold commercially in any format or medium without the formal permission of the copyright holders.

This document is the author's post-print version, incorporating any revisions agreed during the peer-review process. Some differences between the published version and this version may remain and you are advised to consult the published version if you wish to cite from it.

Removal of Arsenic and Metals from Groundwater Impacted by Mine Waste Using Zero-valent Iron and Organic Carbon: Laboratory Column Experiments

Joanne U. Angai^a, Carol J. Ptacek^a, Eva Pakostova^{a,b}, Jeff G. Bain^a, Brent R. Verbuyst^a, David W. Blowes^a

^aDepartment of Earth and Environmental Sciences, Faculty of Science, University of Waterloo, Waterloo, Ontario, Canada.

^bFaculty Research Centre for Sport, Exercise and Life Sciences, Faculty of Health and Life Sciences, Coventry University, Coventry, UK.

Corresponding author

Dr. Carol Ptacek

Address: Department of Earth and Environmental Sciences, Faculty of Science, University of Waterloo, Waterloo, Ontario, Canada.

Phone: +1 519-888-4567 ext. 32230

Email: ptacek@uwaterloo.ca

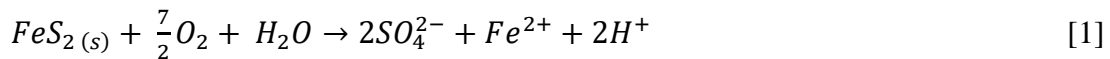
Abstract

Acid mine drainage and the associated contaminants, including As and metals, are an ongoing environmental issue. Passive remediation technologies have the potential to remove As from mine waste effluents. A series of laboratory column experiments was conducted to evaluate the effectiveness of varying mixtures of organic carbon (OC), zero-valent iron (ZVI), and limestone for the treatment of As, metals, SO_4^{2-} , and acidity in groundwater from an abandoned gold mine. The onset of bacterially-mediated SO_4^{2-} reduction was indicated by a decrease in Eh, a decline in aqueous SO_4^{2-} concentrations coupled with enrichment of $\delta^{34}\text{S}$, and the presence of sulfate-reducing bacteria and H_2S . Removal of As was observed within the first 3 cm of reactive material, to values below $10 \mu\text{g L}^{-1}$, representing >99.9% removal. An increase in pH from 3.5 to circumneutral values and removal of metals including Al, Cu, and Zn was also observed. Synchrotron results suggested As was removed through precipitation of As-crystalline phases such as realgar and orpiment, or through adsorption as As(V) on ferrihydrite. The results indicate the potential for a mixture of OC and ZVI to remove As from acidic, mine-impacted water.

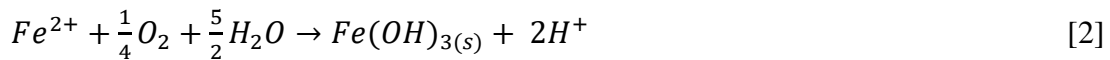
Keywords: Mining, permeable reactive barriers, water treatment, acid mine drainage

1. Introduction

One of the major sources of arsenic (As) in groundwater is mining. Gold (Au) mining in particular results in large amounts of As in wastes because As-bearing minerals are commonly present in Au-bearing ore bodies. During mining, rock is excavated to access the ore bodies, resulting in the production of large volumes of waste rock. Processing to concentrate valuable metals results in the production of fine-grained mill tailings that are typically deposited into impoundments. Arsenic occurs in waste rock and tailings in the form of gangue minerals and recalcitrant sulfide ore, including arsenopyrite (FeAsS), arsenian pyrite (As-rich FeS₂), and As-bearing Fe oxyhydroxides (Blowes et al., 2014). Unmanaged tailings deposits and waste-rock piles are of particular concern due to the potential for the oxidation of sulfide minerals (Blowes et al., 2014):



and the oxidation of ferrous Fe:



H⁺ is released in the above reactions, resulting in increased acidity. Sulfate (SO₄²⁻) and metal(loid)s are also released into groundwater during oxidation processes (Blowes et al., 2014; Evangelou and Zhang, 1995). Tailings deposits can be of concern due to the potential to leach metals and metalloids into nearby water systems, resulting in contaminated acidic water that can persist for decades or centuries (Blowes and Jambor, 1990; Blowes et al., 2014; Moncur et al., 2005; Sprague et al., 2016). Migration of fugitive tailings downstream may result in the dispersion of metal(loid)-rich water and sediment into nearby environments, especially in cases

where migration does not result in reduced toxicity (Sprague et al., 2016). Leaching of contaminated groundwater is especially prevalent at mine sites where the tailings are deposited without engineered containment. In carbonate-rich systems, low pH acidic drainage is often neutralized (Blowes et al., 2014). However, after the neutralization capacity is exceeded, the pH may decrease and the concentrations of other contaminants may again increase. Such acidic waters can pose a health risk to humans and organisms living nearby.

An established approach for the remediation of As-contaminated groundwater is permeable reactive barriers (PRBs). PRBs are passive, *in situ* barriers placed within the subsurface directly in the path of groundwater flow and contaminant transport (Blowes et al., 1998). The barrier is filled with material that reacts with the target contaminant. PRBs utilize processes such as adsorption, precipitation, and reduction to effectively remove and stabilize contaminants.

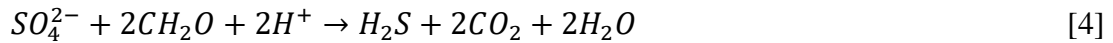
Zero-valent iron (ZVI) is often used in environmental remediation. Several laboratory studies have examined the processes by which ZVI removes As from water (Bain et al., 2002; Biterna et al., 2007, 2010; Lien and Wilkin, 2005; Su and Puls, 2001). Anaerobic corrosion of ZVI by water releases Fe(II) through (Gould, 1982):



The release of Fe(II) allows for solid phases such as Fe (oxy)hydroxides and ferrous hydroxy carbonate to form (Jeen et al., 2007), which create highly reactive surface sites to which As can adsorb, and allows for retention of both As(III) and As(V) (Bang et al., 2005; Ludwig et al., 2009; Su and Puls, 2001). Furthermore, As can co-precipitate with green rust (Lien and Wilkin, 2005), which incorporates into the structure of pyrite during SO_4^{2-} reduction (Blowes et al., 2014) and, over time, may result in a more effective PRB (Su and Puls, 2001). Previous

laboratory studies confirm the effectiveness of ZVI for removing As from water through co-precipitation and adsorption processes.

Organic carbon (OC) is another reactive material often utilized for environmental remediation. The addition of OC substrates promotes the growth and activity of sulfate-reducing bacteria (SRB) and results in bacterially-mediated SO_4^{2-} reduction (Benner et al., 1997):



The hydrogen sulfide produced reacts with soluble metals (Me) to form metal sulfide minerals (Ludwig et al., 2002):



In addition to reaction [5], other elements such as As can react with H_2S to form sulfide minerals (Benner et al., 1997). If As-bearing sulfide minerals are precipitated in an environment where O_2 is limited, As is effectively immobilized provided the system remains anaerobic and oxidation reactions are limited. Such environments include fully saturated locations, such as tailings ponds. Past experiments have utilized OC in the form of compost, wood chips, and leaf compost (Benner et al., 1997; Lindsay et al., 2011b; Ludwig et al., 2009; Waybrant et al., 2002). Furthermore, varied mixtures of OC sources have been found to be more effective for contaminant removal as opposed to a single source (Waybrant et al., 1998, 2002).

Long Lake is an abandoned Au mine, near Sudbury, Ontario (**Figure A.1**), with elevated metal(loid) concentrations in groundwater and tailings porewater. All of the tailings produced during the milling process were deposited into three tailings areas (**Figure A.2**) and capped with a layer of sand (CH2MHill, 2014). The downstream migration of tailings has led to the formation of a tailings delta at the southwestern end of Long Lake. Arsenic is the primary contaminant of

concern in the Long Lake tailings impoundment. Elevated concentrations of SO_4^{2-} as well as Fe, Al, and other metals are also observed.

Although several studies have explored the effectiveness of OC and ZVI for the removal of As and other metal(loid)s from mine-impacted water (Guo & Blowes, 2009; Jeon et al., 2014; Pagnanelli et al., 2009), there is limited information on the potential for these materials to sustain low concentrations of As under acidic conditions with pH values as low as 3. Groundwater from the Long Lake tailings is unique due to its low pH and high As and metal concentrations. To increase the understanding of the mechanisms contributing to contaminant removal under these challenging conditions, synchrotron-based techniques (bulk XANES, μ XANES, μ XRF) to evaluate As and S speciation have been integrated with culture-dependent and culture-independent techniques to investigate the underlying microbial processes.

2. Materials and Methods

2.1 Column Design and Experimental Setup

Four acrylic columns (30 cm long, 5 cm internal diameter) were used for the column experiments and named T0, T1, T2, and T3, respectively. Different mixtures were tested to study the influence of OC on the efficacy of SO_4^{2-} reduction and overall treatment. Each was filled with various quantities of reactive material (**Table 1**), composed of silica sand (SS) (U.S. Silica Company), pulverized limestone (Beachville Quarries), granular ZVI (Connelly-GPM), and OC in the form of composted leaf mulch and wood chips (Waterloo Regional Landfill) obtained in the summer of 2018. The silica sand particles ranged from 0.60 mm to 1.18 mm (20-30 standard sand ASTM C778) and the ZVI particles were predominantly in the 0.30 mm to 2.36 mm size range. The mixture of OC and ZVI was thoroughly mixed with silica sand, to increase

permeability, and limestone, to neutralize the acidic pore water. The characteristics of the reactive material used for the mixtures are summarized in **Table A.1**. Approximately 2 g of organic-rich sediment collected from Laurel Creek, Waterloo was spread throughout each of the four columns during packing to enhance the growth of bacterial populations in the reactive material. Each column was fit with an influent and effluent port, 13 water sampling ports spaced at 2-cm intervals along the length of one side of the column, and 8 larger solid sampling ports spaced at 3.25-cm intervals along the opposite side of the column. A 3-cm layer of nonreactive silica sand was placed at both the influent and effluent ends of the column to separate the reactive mixture from the end ports (**Figure A.3**; Liu et al., 2014). The layers of silica sand were bounded by coarse- and fine-mesh NITEX™ screens. Prior to the start of groundwater pumping, the columns were flushed with CO₂ gas to displace the air within the columns.

A feed solution with 5% Na-lactate and 1000 mg L⁻¹ SO₄²⁻ was then pumped through the columns to saturate the reactive material (Waybrant et al., 2002). Post-saturation, the influent and effluent ends of the columns were clamped before the columns were transferred into an anaerobic chamber and left for 12 d to allow the growth of bacterial populations. The columns were then subjected to continuous pumping of As-bearing groundwater collected from the Long Lake site. Water was pumped from the bottom upwards through the columns at an average rate of 3.24 mL h⁻¹ using a multi-channel peristaltic pump (Ismatec and Rainin Dynamax). The flow rate of the columns was approximately three times the flow rate of groundwater near the source piezometer. The influent water was collected monthly from the site to reduce any potential changes in the As(III):As(V) ratio during storage. Part way through the experiments, it became apparent that As was precipitating from the influent water before it was pumped through the columns. A spike of As(III) and FeSO₄ was used to increase the As and Fe concentrations going

into the columns. The influent water was sampled every week to confirm the composition of the groundwater and ensure no major changes in geochemistry had occurred. The average chemical composition of the influent solution is shown in **Table A.2**. The column experiments were conducted for 30 (to 32) weeks. During this time, a number of pore volumes (PVs) passed through each column (60 PVs for T0, 35 PVs for T1, 52 PVs for T2, and 51 PVs for T3; **Table 1**). The influent PVs for all graphs correspond to the PVs from column T0.

Table 1. Mean composition (dry wt. %), flow rate, residence time, porosity, and total pore volumes passed through each column.

Column Name	Organic Carbon (wt. %)	Zerivalent Iron (wt. %)	Silica Sand (wt. %)	Limestone (wt. %)	Avg Flow Rate (mL h ⁻¹)	Residence Time (d)	Total PV	Porosity
T0 0:0	0	0	90	10	3.0	3.69	59.9	0.37
T1 40:10	40	10	45	5	3.1	6.41	34.5	0.64
T2 30:20	30	20	45	5	3.4	4.67	52.3	0.47
T3 20:30	20	30	45	5	3.4	4.59	50.9	0.45

2.2 Sample Collection

2.2.1 Effluent/Influent and Port Sampling

Water sampling took place directly in the glovebox. Collection of effluent and influent samples was conducted approximately once a week; secondary sampling was conducted four to five times over the course of the experiment. Effluent and influent sampling included the collection of samples for pH, Eh, alkalinity, and determination of the concentrations of cations, anions, nutrients (NH₄-N and PO₄-P), and dissolved H₂S. Secondary sampling included the collection of water for the determination of dissolved organic carbon (DOC), dissolved inorganic carbon

(DIC), carbon isotopes, and sulfur isotopes. To assess changes in geochemistry along the length of the columns, two profiles were collected over the course of the experiment. Profile samples were collected using a glass syringe starting at the effluent end of the column moving downwards, to prevent disturbance to flow. Water samples were collected from the effluent ports using 100-mL amber glass bottles that were connected using 0.32-cm outer diameter Teflon tubing and 0.32-cm outer diameter Pharmed® BPT tubing to 1-L polyethylene and amber bottles. All samples were collected using syringes and passed through a 0.45- μ m filter (Acrodisc®) into polyethylene bottles. Samples were preserved with 67-70% OmniTrace® HNO₃ for analysis of cations and trace elements and with 95-98% A.C.S. Reagent H₂SO₄ for DOC and nutrient analyses, to a pH < 2. Samples for anions, DIC, $\delta^{13}\text{C}$, and $\delta^{34}\text{S}$ were not acidified. Samples for analysis of DIC were frozen prior to analysis. All other samples were refrigerated.

2.2.2 Solid-phase Sampling

Prior to removing solid material from the columns, the pumps were turned off and both ends of the column were clamped to prevent water from entering or leaving. Each column was placed horizontally with the solid sampling ports facing upward (**Figure A.3**). Ports were opened one at a time and material (12-15 g) removed using a sterilized metal scoopula, then placed in centrifuge tubes. The columns were then opened from the top and sectioned every 3 to 5 cm and material samples were placed in 20-mL glass vials. The glass bottles were sealed with vinyl tape and stored in the freezer until sample analysis.

2.3 Analytical Methods

2.3.1 Aqueous Analysis

The pH (Orion 3 Star meter connected to an Orion 815600 Ross Combination pH Probe) and Eh (Orion 3 Star meter connected to an Orion 9678B NWD Sure-Flow Combination redox electrode) were measured immediately after collection on unfiltered samples. The pH electrode was calibrated daily using pH 4, 7, and 10 buffers (traceable to NIST). The Eh electrode was checked for response against Zobell's and Light's solutions prior to sampling. Alkalinity (Hach digital titrator and bromocresol green-methyl red indicators; Method 10244 from the HACH Hydraulic Fracturing Water Analysis Handbook, Edition 8) was measured immediately on filtered samples.

Samples from the water sampling ports, as well as influent- and effluent-water samples, were analyzed at the University of Waterloo, Groundwater Geochemistry and Remediation Laboratory, to determine concentrations of dissolved cations (inductively-coupled plasma mass spectrometry, Thermo Fisher Xseries II; inductively-coupled plasma optical emissions spectroscopy, Thermo Fisher iCAP 6000), dissolved anions (ion chromatography, Dionex IC-CO₃), and DIC and DOC (total organic carbon method, Aurora 1030 TOC Analyzer). Using a spectrophotometer (HACH DR 2800), concentrations of dissolved aqueous sulfide were measured using the methylene blue spectrophotometric method (Method 8131, DR 2800 Manual), NH₃-N using the salicylate method (Method 10031/10032, DR 2800 Manual), and PO₄-P using the ascorbic acid method (Method 8048, DR 2800 Manual).

2.3.2 *Environmental Isotopes*

Samples for determination of $\delta^{13}\text{C}$ were collected in 40-mL amber glass bottles and kept in the freezer prior to analysis by the Environmental Isotope Laboratory at the University of Waterloo. Samples for $\delta^{34}\text{S}$ were collected in polyethylene bottles and kept in the fridge until analysis prior to submission to the Isotope Science Laboratory at the University of Calgary where BaSO_4 was precipitated out of the sample before being analyzed for $\delta^{34}\text{S}$.

2.3.3 *Carbon-Sulfur Analyzer*

Samples for C/S measurements were anaerobically freeze-dried prior to analysis using an ELTRA CS 2000 Carbon Sulfur Determinator. After freeze-drying, the samples were transferred into an anaerobic chamber. A magnet was used to separate ZVI and dust from the OC. Due to the large variability in the reactive material (limestone, wood chips, leaf compost, etc.) and the inability to separate all components, measured C was determined to not provide an accurate representation of the C content. Therefore, only the S wt. % was used.

2.3.4 *Culturable Heterotrophic Microorganisms*

Microbiological analyses using the most probable number (MPN) technique were conducted on solid samples to enumerate SRB and neutrophilic heterotrophs (nH). For SRB, triplicate solid samples (1 g) were added to 20-mL serum bottles that contained 9 mL of a modified Postgate C medium (Postgate, 1984), which was at a pH of 7.5 and contained 2.92 g L^{-1} Na-lactate (60%), 1.28 g L^{-1} Na acetate, and a resazurin supplement to indicate anaerobic conditions (Benner et al., 1999; Lindsay et al., 2008; Paulson et al., 2018). Following the MPN technique, the serum bottles were serially diluted (Gould et al., 2003). After being inoculated, the bottles were incubated in an anaerobic chamber for 5 weeks, after which inspection of the serum bottles

commenced. The presence of a black precipitate indicated biogenic H₂S production via SO₄²⁻ reduction. Populations of SRB were counted following the MPN technique (Cochran, 1950). For nH, each sample was serially diluted and plated onto R2A agar (Sigma Aldrich, USA). The plates were incubated aerobically at room temperature (~23 °C) without agitation. After 7 d, the colony forming units were counted. Duplicates were determined by two successive dilutions that showed colony growth.

2.3.5 DNA Extraction and Illumina MiSeq Sequencing

Total genomic DNA was extracted in duplicate using DNeasy PowerSoil Kits (Qiagen Inc., Germany) on solid samples stored at -20 °C. DNA samples were submitted for 16S rRNA gene amplicon sequencing to Metagenom Bio Inc. (Toronto, Canada). The modified universal primers 515F/806R (Walters et al., 2015) were used to amplify the V4 region of 16S rRNA genes, followed by Illumina MiSeq sequencing. Sequencing data were processed using the Mothur program v.1.39.5 (Schloss et al., 2009) and Mothur MiSeq Standard Operating Procedure (Kozich et al., 2013), as described by Pakostova et al., 2020. In short, clustering of operational taxonomic units (OTUs) was conducted at a 97% similarity level using a *de novo* OTU picking process and the Silva database (release 132 for Mothur, downloaded 18/03/2019) was used as a reference for taxonomic annotation. Relative abundances of sulfate-reducing bacteria (SRB) were obtained by screening the taxonomy file for prokaryotic genera (or in a few instances higher taxa when identification to the genus level was not possible) containing at least one species with the investigated metabolic trait. **Table A.3** shows a list of SRB detected in the samples, as well as their mean % of total reads (in the whole data set, not individual samples).

2.3.6 Light Microscopy and SEM

Subsamples of the solids collected from the columns were sent to Spectrum Petrographics (Vancouver, Washington) for thin section preparation. Samples were anaerobically freeze-dried prior to submission and stored in an anaerobic chamber to prevent exposure to atmospheric O₂. Double-sided, polished, thin sections were prepared by mounting samples with Krazy Glue® onto a Suprasil 2A quartz plate. These slides were suitable for synchrotron-based μ X-ray fluorescence (μ XRF) and μ X-ray diffraction (μ XRD) analyses.

Thin sections were examined under both reflected and transmitted light using a Nikon Eclipse LV100N POL polarized light microscope to identify OC and ZVI grains. Grains of interest were marked on the slide and analyzed to determine the percentage of elements in the grain using scanning electron microscopy (SEM) and electron dispersion X-ray analysis (EDX) (Hitachi TM3000 Tabletop SEM coupled with a Bruker QUANTAX 70 EDS).

2.3.7 Synchrotron Analyses

Thin sections were analyzed using synchrotron μ XRF mapping of As on beamline 20-ID at the Advanced Photon Source (APS) in Lemont, Illinois. Locations of interest on the grain were further analyzed for As μ X-ray absorption near edge structure (μ XANES). Synchrotron μ XRF mapping of S was conducted on one thin section using beamline SXRMB at the Canadian Light Source (CLS) in Saskatoon, Saskatchewan. Points of interest on the grain were analyzed with S μ XANES.

Samples of ZVI prepared for bulk S XANES analyses at the CLS were collected from the column under anaerobic conditions and then frozen in liquid N₂. The frozen samples were

crushed under anaerobic conditions using a mortar and pestle, to remove grain coatings, sieved, and stored in 2-mL vials which were kept in an anaerobic chamber before transport to the CLS. Processing of μ XANES, XANES, and μ XRF data was carried out using the program ATHENA (Ravel and Newville, 2005). Two to four scans were merged in $\mu(E)$ to reduce noise and create data that were easier to fit and interpret. In cases where beam damage was apparent, only the first scan was used. The merged scans were energy shifted with respect to the reference standard gypsum, that was collected during the same beamline time. Linear combination fitting (LCF) of (μ)XANES provides a quantitative assessment of the species and, in some cases, can predict the phases present in the solid material to ± 5 -10 % (Foster and Kim, 2014).

2.3.8 Data Interpretation

Removal of As from all four columns was calculated from the cumulative mass in the column influent minus the cumulative mass in the column effluent. Mass removal was based on weekly gravimetric determinations of water volume combined with analytical determinations of As concentrations. Sulfate removal rates were calculated for each of the treatment columns (T1, T2, and T3). The best-fit SO_4^{2-} reduction equation was based on observed SO_4^{2-} removal for each column (SigmaPlot, SPSS Inc.). The rates were further normalized to per weight (g) of dry OC (Lindsay et al., 2008; Waybrant et al., 1998). Data from the column experiments were input into the geochemical modelling software PHREEQCI using the WATEQ4F (Ball and Nordstrom, 1991) database to determine the saturation indices.

3. Results

3.1 Water Chemistry

3.1.1 Geochemical Conditions

The geochemical conditions in treatment columns T1, T2, and T3 exhibited similar characteristics in terms of effluent pH, Eh, and alkalinity (**Figure 1**). Due to differences in reactive materials and column packing the pore volume and velocity differed between the columns (Table 1). Column 1 had the greatest pore volume and lowest velocity, whereas Column T0 had the smallest pore volume and the greatest velocity. The column residence times varied from 3.69 d (Column T0) to 6.41 d (Column 2), For simplicity, the influent water chemistry is plotted relative to the residence time of Column T0. The influent water pH remained at a mean value of 3.5 throughout the experiment; mean effluent pH values were 7.3, 7.6, and 7.9 for T1, T2, and T3, respectively. Column T0 (0 wt. % ZVI) exhibited similar pH values, with a mean effluent of 7.2. A sharp initial increase in pH within the first 3 cm was observed in all four columns (**Figure 2**). The mean influent Eh value was 406 mV, and column effluents had a mean Eh of 32, 5, -5, and -27 mV for T0 to T3, respectively. A sharp initial decrease in Eh was observed in all four columns within the first 3 cm of reactive material but subsequent Eh values remained near 0 mV (**Figure 2**). Effluent alkalinity was initially high in the first 5 PVs of flow, then tapered off to lower, more constant, values after approximately 6 PVs. The mean influent alkalinity was close to 0 mg L⁻¹ as CaCO₃ and the four column effluents had mean values of 1870, 2610, 2140, 2230 mg L⁻¹ as CaCO₃ for the first 5 PVs, and 163, 278, 248, 251 mg L⁻¹ as CaCO₃ for the remainder of the experiment (T0 to T3; **Figure 1**). A substantial increase in alkalinity along the length of the column occurred early in the experiment (**Figure 2**). Near the

end of the experiment, the magnitude of alkalinity increase was lower. The mean alkalinity in all four columns, not including the initial increase, was close to 100 mg L⁻¹ as CaCO₃.

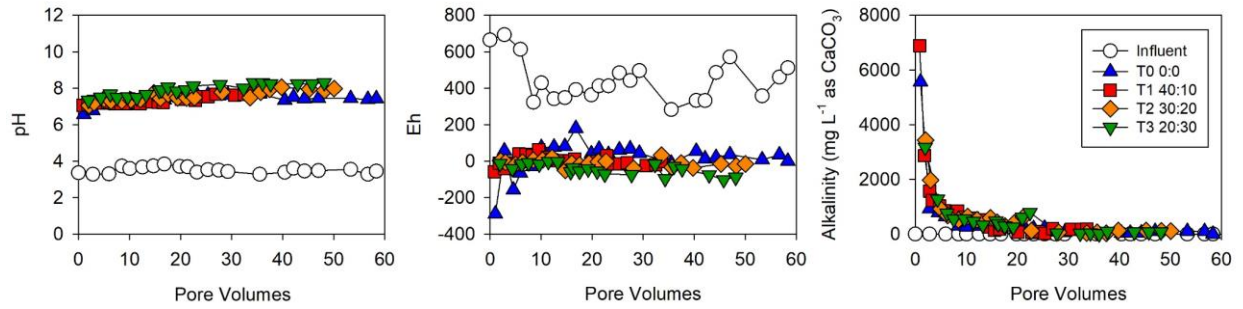


Figure 1. pH, Eh, and alkalinity versus number of PVs in the influent and effluent of the four columns.

The OC:ZVI ratio in column T0 is 0:0, T1 is 40:10, T2 is 30:20, and T3 is 20:30.

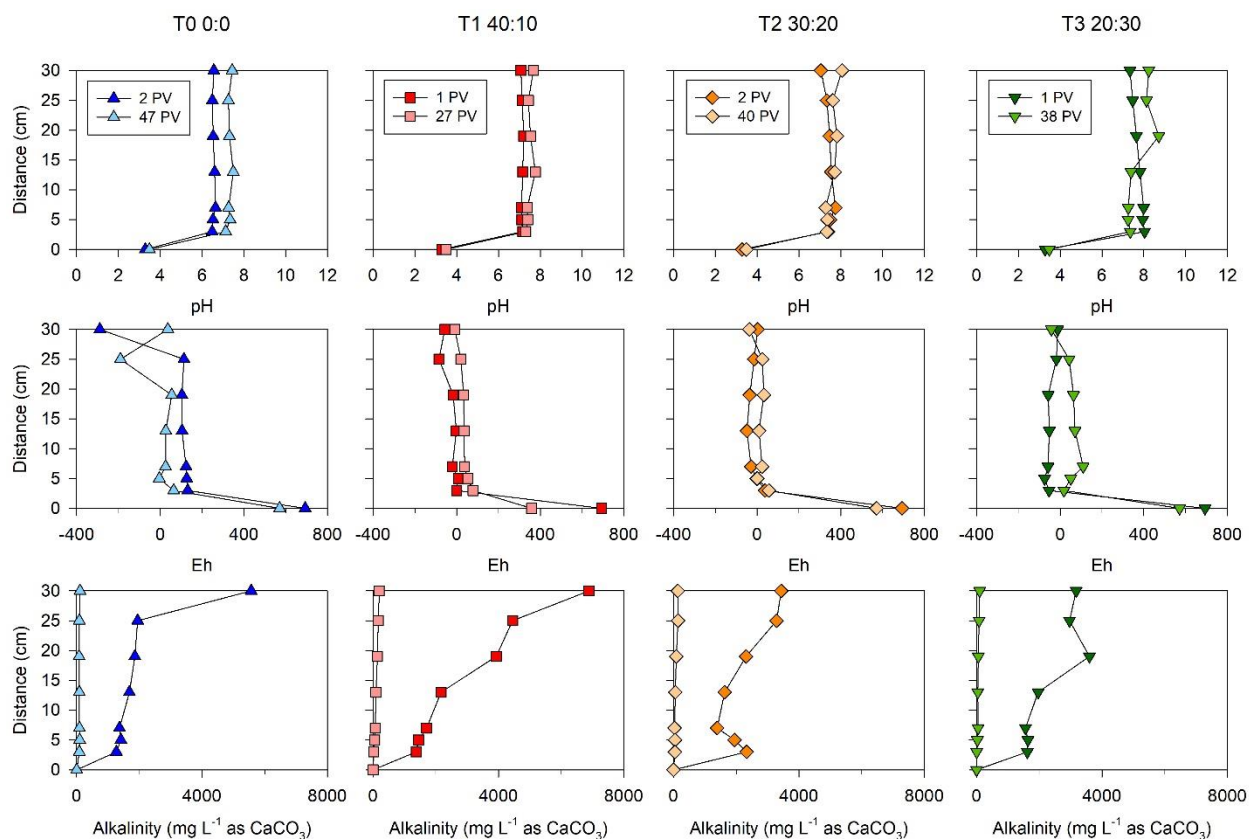


Figure 2. pH, Eh, and alkalinity in aqueous samples collected along the length of columns T0, T1, T2, and T3 at two different time points. Each column of graphs represents a different experimental column. Distance 0 cm represents the influent concentration and 30 cm represents the effluent concentration. The OC:ZVI ratio of column T0 is 0:0, T1 is 40:10, T2 is 30:20, and T3 is 20:30.

3.1.2 As

The concentrations of As in the influent water were as high as 10 mg L⁻¹ (**Figure 3**). The influent As concentration declined sharply at 21 PVs and remained low until 35 PVs, at which time As and Fe were added to the influent water. From 8 to 21 PVs, the As concentration varied between 2000 and 5500 µg L⁻¹ (**Figure 3**). After 21 PVs, the concentration declined to between 20 and 270 µg L⁻¹. Variations in influent As concentration occurred over the course of the experiment, likely due to O₂ exposure. During storage of water from the time of collection until use,

precipitation of As occurred, resulting in variable influent concentrations. Because of this, the influent solution was spiked to 6800-9600 $\mu\text{g L}^{-1}$ As from 35 PVs until the conclusion of the experiment.

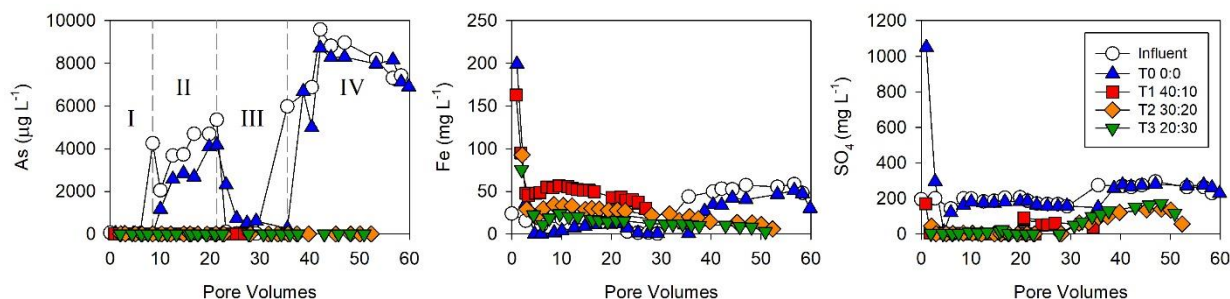


Figure 3. Concentrations of As, Fe, and SO_4^{2-} versus number of PVs in the influent and effluent of the four columns. Input of As was discontinuous throughout the experiment, with concentrations varying between four main stages (left). A spike of As and Fe was added at the third grey dashed line (35 PVs) following the end of stage III. The OC:ZVI ratio of column T0 is 0:0, T1 is 40:10, T2 is 30:20, and T3 is 20:30.

Mean As concentrations in the column effluents were 3.6 mg L^{-1} , $3.9 \mu\text{g L}^{-1}$, $2.7 \mu\text{g L}^{-1}$, and $2.2 \mu\text{g L}^{-1}$ for columns T0 to T3, respectively. The first column profile was collected following the initial flush of groundwater through the reactive columns. During this time, As concentrations going into the columns were low ($57.5 \mu\text{g L}^{-1}$ for T0/T1; $16 \mu\text{g L}^{-1}$ for T2/T3). Despite low concentrations, all four columns showed a decrease in As concentrations upon reaching the first sampling port (**Figure 4**). Arsenic concentrations dropped below $10 \mu\text{g L}^{-1}$ in T1, T2, and T3 but not T0. The second column profile was collected near the end of the experiments after 47, 27, 40, and 38 PVs for T0 to T3, respectively. The mean As concentration in the column influent was 8.9 mg L^{-1} . Pronounced removal of As was observed within the first 3 cm of T1, T2, and T3, whereas As concentrations remained elevated throughout the column length in T0 (**Figure 4**).

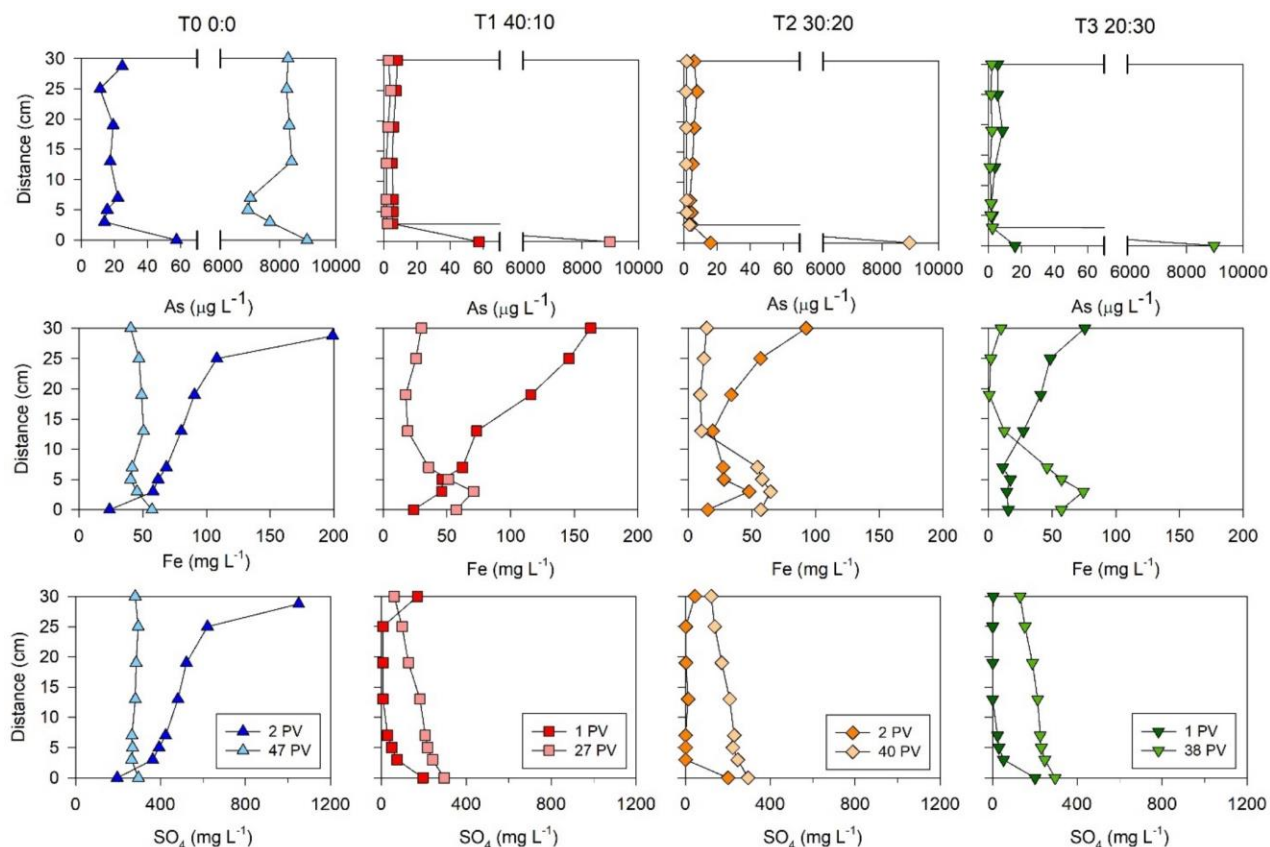


Figure 4. Concentrations of As, Fe, and SO_4^{2-} in aqueous samples collected along the length of columns T0, T1, T2, and T3 at two different time points. Each column of graphs represents a different experimental column. Distance 0 cm represents the influent concentration and 30 cm represents the effluent concentration. The OC:ZVI ratio of column T0 is 0:0, T1 is 40:10, T2 is 30:20, and T3 is 20:30.

3.1.3 Fe

The influent Fe concentration ranged from 11 to 58 mg L^{-1} , with a mean of 13.6 mg L^{-1} prior to the FeSO_4 spike, and a mean of 52.3 mg L^{-1} following the addition of FeSO_4 (**Figure 3**). Starting at 35 PVs, dissolved Fe(II), as FeSO_4 , was added to the influent, increasing concentrations to between $45\text{-}60 \text{ mg L}^{-1}$. The mean concentrations of Fe in the column effluents of T0, T1, T2, and T3 were $26.1, 50.0, 26.2,$ and 16.8 mg L^{-1} , respectively (**Figure 3**). Column profile chemistry samples were collected two times during the experiment (**Figure 4**). The early profile showed an

increase in Fe concentrations along the length of all columns. A larger change in concentration between the profile influent and effluent was observed in columns T0 and T1 (25 to 200 mg L⁻¹), whereas the change was less pronounced in columns T2 and T3 (25 to 100 mg L⁻¹). The second profile, collected at a later PV, showed the opposite trend. Iron concentrations decreased along the column length in all four columns, with T3 and T2 exhibiting the largest decrease in Fe concentrations along the column length, followed by T1 and then T0 (**Figure 4**).

3.1.4 Non-ferrous Transition Metals

The mean influent concentrations of dissolved metals varied (6.8 mg L⁻¹ Al, 0.25 mg L⁻¹ Co, 0.23 mg L⁻¹ Ni, 0.14 mg L⁻¹ Cu, 0.27 mg L⁻¹ Zn, and 0.31 µg L⁻¹ Cd; **Figure 5**). The effluent metal concentrations were less than 5 µg L⁻¹, except for Al which was < 25 µg L⁻¹ for all columns. A sharp decrease in Al, Cu, and Co within the first 3 cm of reactive material was observed in columns T1, T2, and T3, followed by constant values for the remainder of the column length (**Figures A.4, A.5**). Profiles of Ni, Cd, and Zn concentrations show a sharp initial decrease, followed by variable concentrations along the length of columns T1, T2, and T3. Similarly, a sharp initial decrease was observed in column T0 for Al and Cu after which concentrations remained constant for the remainder of the column. For Zn and Cd in column T0, a similar trend to Al and Cu was observed at 47 PVs but, at 2 PVs, the concentrations were variable throughout the column length, with concentrations decreasing at the effluent end. Concentrations for Co and Ni progressively decreased along the length of column T0 (**Figure A.4**).

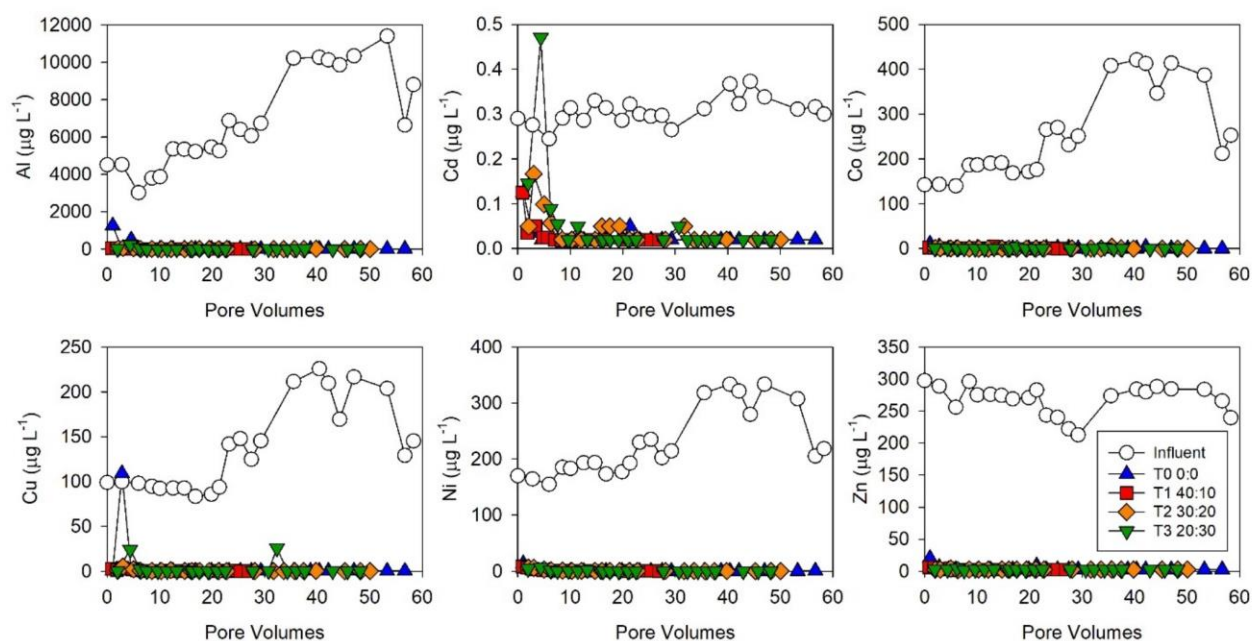


Figure 5. Concentrations of metals (Al, Cd, Co, Cu, Ni, and Zn) versus PVs in the influent and effluent of the four columns. The OC:ZVI ratio of column T0 is 0:0, T1 is 40:10, T2 is 30:20, and T3 is 20:30.

3.1.5 Sulfur Geochemistry

Both SO_4^{2-} and dissolved aqueous sulfide ($\text{S}^{2-}/\text{H}_2\text{S}$) concentrations were measured in the column influent and effluent (**Figure 6**). The mean influent SO_4^{2-} concentration was 214 mg L^{-1} . The mean column effluent SO_4^{2-} concentrations were 236, 26.2, 42.2, and 49.7 mg L^{-1} for T0 to T3, respectively. Port measurements for columns T1, T2, and T3 showed similar rates of SO_4^{2-} removal for both profile sampling episodes (**Figure 4**). The first profile sampling episode showed a sharp initial decrease in SO_4^{2-} , prior to reaching the first sampling port, with no further decline over the remainder of the column length. The decrease in SO_4^{2-} concentrations was more gradual during the second profile episode, measured toward the end of the experiment. The opposite trend was observed at 2 PVs for T0, with SO_4^{2-} concentrations increasing substantially

along the column length. At 47 PVs, SO_4^{2-} concentrations decreased minimally, remaining relatively constant along the column length.

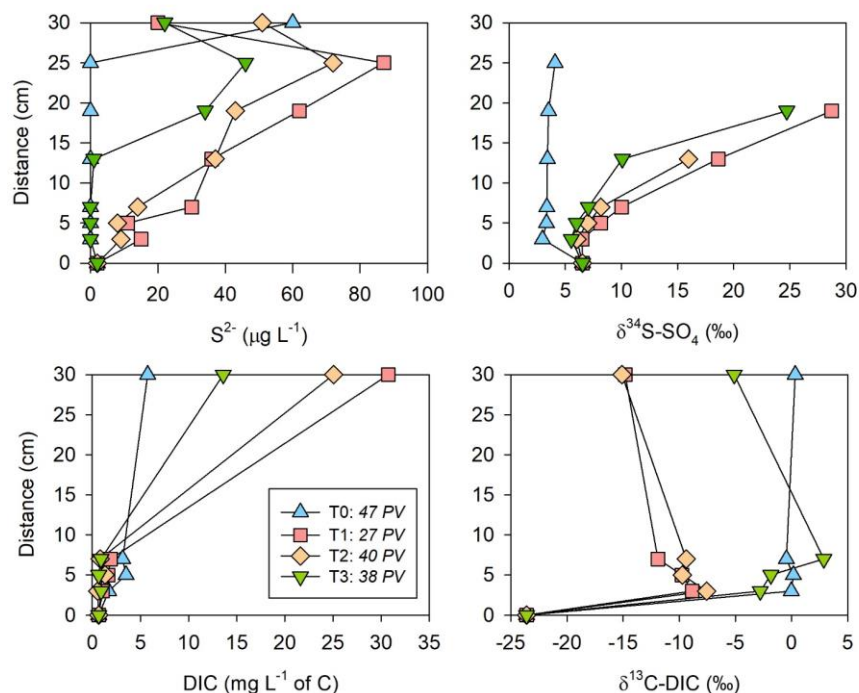


Figure 6. Top row: Concentrations of S^{2-} compared to $\delta^{34}\text{S-SO}_4$ values in aqueous samples collected along the length of columns T0, T1, T2, and T3. Bottom row: Concentrations of dissolved inorganic carbon (DIC) are compared to $\delta^{13}\text{C-DIC}$ along the column length. Data are from the second vertical profile collected. The OC:ZVI ratio of column T0 is 0:0, T1 is 40:10, T2 is 30:20, and T3 is 20:30.

The dissolved aqueous S^{2-} concentration in the influent water was relatively low, with a mean concentration of $5.8 \mu\text{g L}^{-1}$ (**Figure A.6**). The mean column effluent S^{2-} concentrations were $>800 \mu\text{g L}^{-1}$ for T0 and 28.0, 31.6, and $39.3 \mu\text{g L}^{-1}$ for T1 to T3, respectively. Column T0 had high initial S^{2-} concentrations in the effluent, with values up to 24mg L^{-1} at 4.5 PVs (**Figure A.6**). The maximum S^{2-} concentrations in the treatment columns were generally much lower than observed in T0. The column profiles for T1, T2, and T3 showed varied concentrations of S^{2-}

along the column in the first collected profile but an increase in S^{2-} along the length of the column in the second profile (**Figure A.7**). The S^{2-} concentrations in both profiles collected for T0 showed very low concentrations of S^{2-} along the column length, which contrasts with the high concentrations observed in the T0 effluent. This discrepancy may be due to the build-up of black, sulfide precipitate in the effluent collection bottle of T0 during the experiment. It is possible that the initial saturation of Na-lactate and flush of groundwater mobilized the organic-rich sediment that had been added to the column during packing. This sediment along with the sulfide precipitate in the effluent bottle may have contributed to the higher S^{2-} concentrations observed in T0 and would explain the discrepancy between the S^{2-} values along the T0 profile and the higher effluent values.

The sulfur isotope ratio of the influent was 6.5 ‰. Sulfur isotope ratios measured along the column length (second profile) showed a progressive enrichment of $\delta^{34}S-SO_4$, with maximum values of 28.7, 16.0, and 24.7 ‰ in T1 to T3, respectively (**Figure 6**). The extent of enrichment may not be properly represented for column T2 because one less measurement was made due to sample limitations. Column T0 demonstrated an initial decrease in $\delta^{34}S-SO_4$ ratio to 3.0 ‰, followed by relatively constant values for the remainder of the column length.

3.1.6 Carbon

High DOC concentrations of up to 6000 mg L⁻¹ as C were observed in all four column effluents during the first 5 PVs, after which concentrations decreased to between 0 and 30 mg L⁻¹ (**Figure A.8**). The highest concentrations of DOC were observed for columns T0 and T1 (6028 and 5764 mg L⁻¹, respectively), followed by T2 and T3 (3330 and 4121 mg L⁻¹, respectively). Profiles collected for all four columns showed an increase in DOC along the column length, followed by a slight decrease in the effluent (**Figure A.8**). A gradual increase in DIC values was observed in

all four columns, with the highest value observed in the effluent of T1 (31 mg L⁻¹ as C), followed by T2 (25 mg L⁻¹ as C) and T3 (14 mg L⁻¹ as C) (**Figure 6**). A slight increase in DIC occurred near the influent end of T0, followed by values of 3-5 mg L⁻¹ as C over the remainder of the column length.

The mean $\delta^{13}\text{C}$ -DIC values for the unreacted column materials were 2.4 ‰ for limestone, -27.1 ‰ for leaf compost, and -24.6 ‰ for wood chips. The $\delta^{13}\text{C}$ -DIC trend displays a negative, depleted $\delta^{13}\text{C}$ -DIC value of -23.6 ‰ in the influent water (**Figure 6**). Sharp increases in $\delta^{13}\text{C}$ -DIC to -8.8 ‰ (T1), -7.6 ‰ (T2), and -2.3 ‰ (T3) were observed within the first 3 cm of reactive material; following this initial increase, gradual decreases in $\delta^{13}\text{C}$ -DIC values were observed along the length of each column. A sharp increase from -23.6 to 0 ‰ $\delta^{13}\text{C}$ -DIC was observed in column T0, after which values remained relatively constant over the remaining length of the column.

3.1.7 Nutrients

The mean influent NH₃-N concentration was 0.85 mg L⁻¹ with a maximum of 1.56 mg L⁻¹ as NH₃-N (**Figure A.6**). In the first 6-7 PVs, the NH₃-N effluent concentrations were up to 6.7, 6.2, and 8.3 mg L⁻¹ as NH₃-N in T1 to T3, respectively. However, after the initial increase, concentrations remained relatively constant at values below 1 mg L⁻¹. The PO₄-P concentrations in the influent ranged from 0.31 to 1.56 mg L⁻¹, with a mean of 0.18 mg L⁻¹ (**Figure A.6**). The column effluent PO₄-P concentrations reached maximum values during the first 13-15 PVs followed by decreases to near 1 mg L⁻¹ as PO₄-P. The highest PO₄-P values observed in T1, T2, and T3 were 3.6, 4.6, and 2.5 mg L⁻¹ as PO₄-P, respectively. Effluent values of NH₃-N and PO₄-P observed for column T0 were similar to the influent. No obvious trends in NH₃-N values were observed along the column length for T0, T2, and T3, but column T1 demonstrated a decrease in

NH₃-N concentrations at around 10 cm, followed by relatively constant concentrations for the remainder of the column (**Figure A.7**). Phosphate profile measurements for all four columns showed a general decrease in PO₄-P from the influent to the effluent (**Figure A.7**).

3.2 Microbiology

3.2.1 Culturable Heterotrophs

Populations of culturable SRB and nH were enumerated in the solid material collected from four locations on each column (**Figure A.9**). SRB populations remained relatively constant between 10² and 10³ bacteria g⁻¹ in columns T1, T2, and T3, while no culturable SRB were detected in column T0. Enumerations of nH bacterial populations for columns T1, T2, and T3 were 10⁶-10⁷ bacteria g⁻¹ and near 10⁴ bacteria g⁻¹ for column T0. No obvious trends in nH populations were observed along the column length for T1, T2, and T3. Column T0 demonstrated a progressive increase in nH populations from the influent to the effluent end (**Figure A.9**).

3.2.2 DNA Analysis

16S rRNA gene amplicon sequencing of the solid material indicated the presence of SRB in all four columns. Of the SRB identified, the five most abundant genera were *Desulfovibrio*, *Desulfobulbus*, *Desulfomicrobium*, *Desulfuromonas*, and *Desulfobacter* (**Figure 7**). The relative abundance of SRB along the column lengths varied between 3.0 and 10.0% (T0), 2.4 and 4.1% (T1), 3.3 and 6.7% (T2), and 4.7 and 6.8% of total reads (T3) (**Figure 7**). In all three treatment columns, the highest total number of reads of SRB was observed closest to the influent end. The most abundant genus in T0 was *Desulfobulbus*, whereas *Desulfovibrio* was the most abundant genus in T1, T2, and T3.

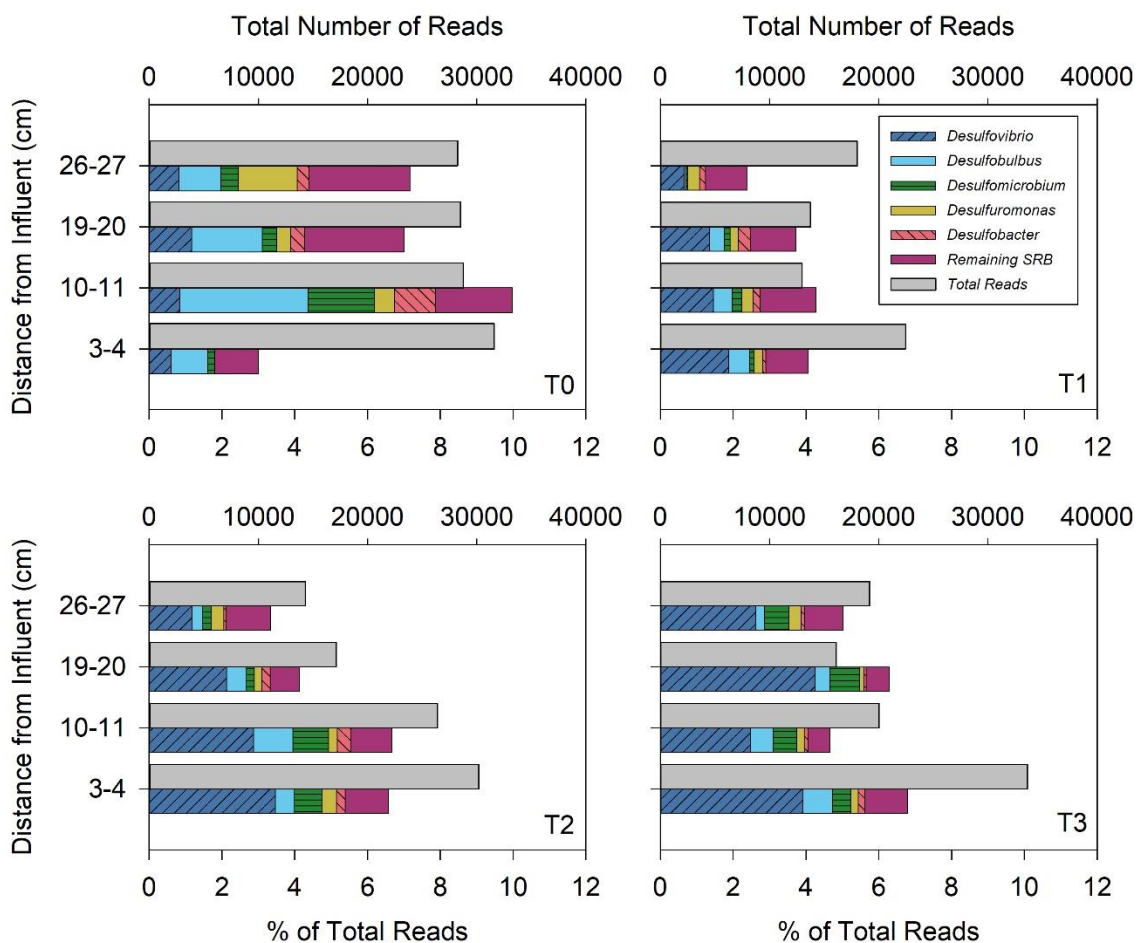


Figure 7. Relative abundance of known SRB identified through 16S rRNA amplicon sequencing in the solid material collected along the length of columns T0, T1, T2, and T3. The five most abundant genera are plotted, and the remaining SRB grouped separately. The total number of reads of SRB obtained during sequencing (top bar) and the percentage of total reads including the distinction between major SRB genera (bottom bar) are shown.

3.3 Mineralogy

3.3.1 Reflected and Transmitted Light Microscopy and SEM

Reflected and transmitted light microscopy was used to identify minerals in the starting materials and in samples collected from the columns at the end of the experiments. Unreacted grains of

ZVI were analyzed to observe the structure and properties of the grains prior to the experiments (**Figure A.10**). This examination was used to distinguish whether reaction rims around the ZVI were due to chemical reactions in the column or if they were present prior to the experiments. Grains of interest were further examined with SEM to determine the dominant elements present in the grain.

The dominant sulfide mineral present in the reactive mixtures at the end of the experiment was pyrite, which occurred as framboids, both as clusters and as individual, isolated framboids. No single crystals or cubes of pyrite were observed. Small amounts of chalcopyrite (CuFeS_2) and pyrrhotite ($\text{Fe}_{(1-x)}\text{S}$) were also observed. Iron sulfide precipitates were observed between grains of silica sand and as rims around the ZVI grains (**Figure A.11**). Internal cell structure was observed in the OC, with occasional infilling by Fe sulfide (**Figure A.12**). The occurrence of both Fe and S in the secondary precipitates was confirmed by SEM-EDX.

Iron (oxy)hydroxides, both as separate grains and as corrosion products on ZVI, were observed. These corrosion products often replaced substantial sections of the ZVI grain and varied in texture.

3.3.2 Solid Sulfur

The average wt. % S content measured in the solid material from the treatment columns was compared to the aqueous SO_4^{2-} concentrations (**Figure A.13**). The S content of unreacted material was 0.12 wt. % for leaf mulch, 0.04 wt. % for wood chips, and 0.15 wt. % for untreated, fresh ZVI. The S content near the influent was 1.1, 1.1, and 0.76 wt. % in T1 to T3, respectively. The greatest mass of S was observed at the influent ends of the columns. A progressive decrease in solid-phase S content was observed toward the effluent end in all three columns. The decrease

in S content was consistent with the observed decrease in dissolved SO_4^{2-} concentrations along the column length. The abundance of S present in the solid material was greatest in column T1, followed by T2 then T3.

3.3.3 Synchrotron-based Bulk S (μ)XANES and S μ XRF Mapping

Synchrotron radiation-based bulk S XANES for the unreacted ZVI (**Figure 8**) indicates the presence of S in two predominant oxidation states: sulfate (2482 eV) and an intermediate, oxidized S species (2476 eV), similar to tetramethylene sulfoxide ($\text{C}_4\text{H}_8\text{OS}$) (Wang et al., 2019). Spectral data indicate S occurs in three oxidation states (a/b, c, d; **Figure 8**) within the solid material from the treatment columns. The adsorption edge of the group designated “a/b” ranges from 2470 to 2472 eV, which is in the range of FeS, elemental S (S_8^0), and/or pyrrhotite (Fleet, 2005). Because the E0 of this group can vary 2 eV between sample spectra, it is not possible to distinguish which reduced S phase is present. The spectral peak indicating a second oxidation state, “c”, occurs at 2476 eV and is in the range of the E0 of an organic, intermediate, oxidized S species. The highest energy edge, “d” occurs at 2482 eV, which is an oxidized sulfate species, likely gypsum ($\text{CaSO}_4 \cdot 2\text{H}_2\text{O}$), based on the E0 of the adsorption edge (Fleet, 2005).

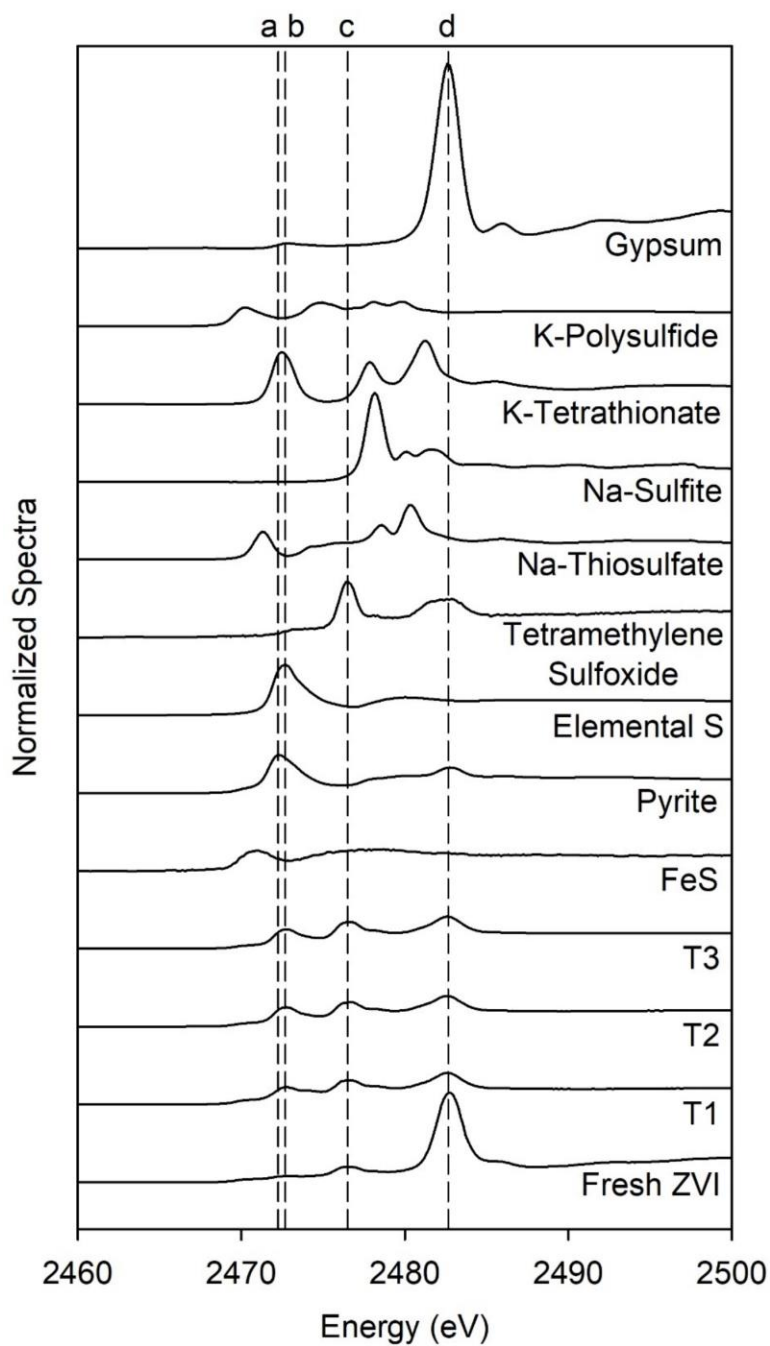


Figure 8. Bulk S XANES spectra of solid samples collected from laboratory columns T1, T2, and T3. Spectra of untreated, fresh ZVI and other standards are also shown. The spectral peak locations for pyrite (a), elemental S (b), tetramethylene sulfoxide (c), and gypsum (d) are shown with dashed lines.

Sulfur μ XRF mapping targeted a grain where a secondary precipitate replaces the cellular organic material, as observed by optical microscopy and SEM (**Figure 9**). The results of sulfur μ XRF analysis indicate S occurs primarily around the rim of the grain and only in localized hotspots in the center of the grain; in contrast, μ XRF indicates Fe is dispersed throughout the grain. Minimal variation is observed in the S μ XANES spectra measured at five locations within the grain showing two major oxidation states (a/b, e; **Figure 9**). The majority of S is present as a reduced phase with an E0 of 2471 to 2472 eV, corresponding to pyrite and elemental S. The second peak located at 2482 eV corresponds to gypsum. A third, lesser component corresponds to intermediate oxidation states (*e.g.*, Na-thiosulfate or K-tetrathionate).

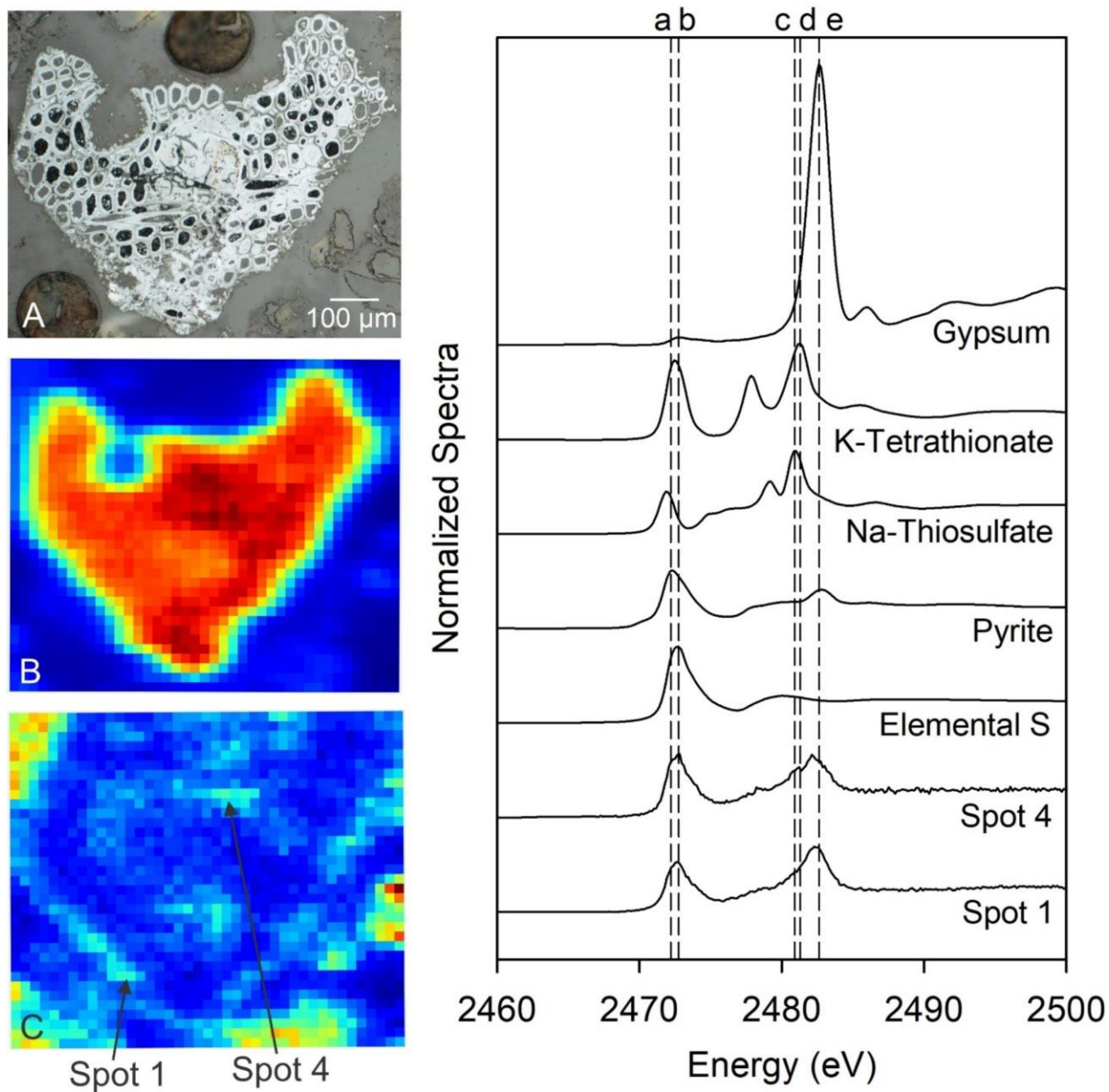


Figure 9. Results from optical microscopy (A), Fe μ XRF imaging (B), S μ XRF imaging (C), and S μ XANES spectra (right) of a secondary precipitate replacing OC substrate. Spectra from two separate scan locations (spots 1 and 4) are plotted with standards used for LCF. The spectral peak locations of pyrite (a), elemental S (b), Na-thiosulfate (c), K-tetrathionate (d), and gypsum (e) are shown with dashed lines.

3.3.4 Synchrotron-based As μ XRF Mapping and As μ XANES

The μ XRF mapping of secondary precipitates indicates the presence of As in grains containing both Fe and S (**Figures 10, A.14**). Arsenic occurs both on the edges of grains and at localized spots rather than uniformly throughout the entire grain. Arsenic μ XANES was collected at a location of relatively high concentration, identified through μ XRF mapping. Two major oxidation states of As are observed as represented by peaks at 11867 to 11878 eV ($-1/+3$) and 11874 to 11875 eV ($+5$). Reduced and oxidized species are present in the solid material at each spot measured, but the majority of As is present in the reduced state. The predominant As species observed in the Fe-S secondary precipitates are consistent with arsenopyrite (FeAsS , -1), orpiment (As_2S_3 , $+3$), realgar (AsS , $+3$), and As(V) sorbed onto ferrihydrite, or possibly as kankite ($\text{FeAsO}_4 \cdot 3.5\text{H}_2\text{O}$) (Walker et al., 2005). The presence of kankite could not be confirmed because of low counts in the spectral data.

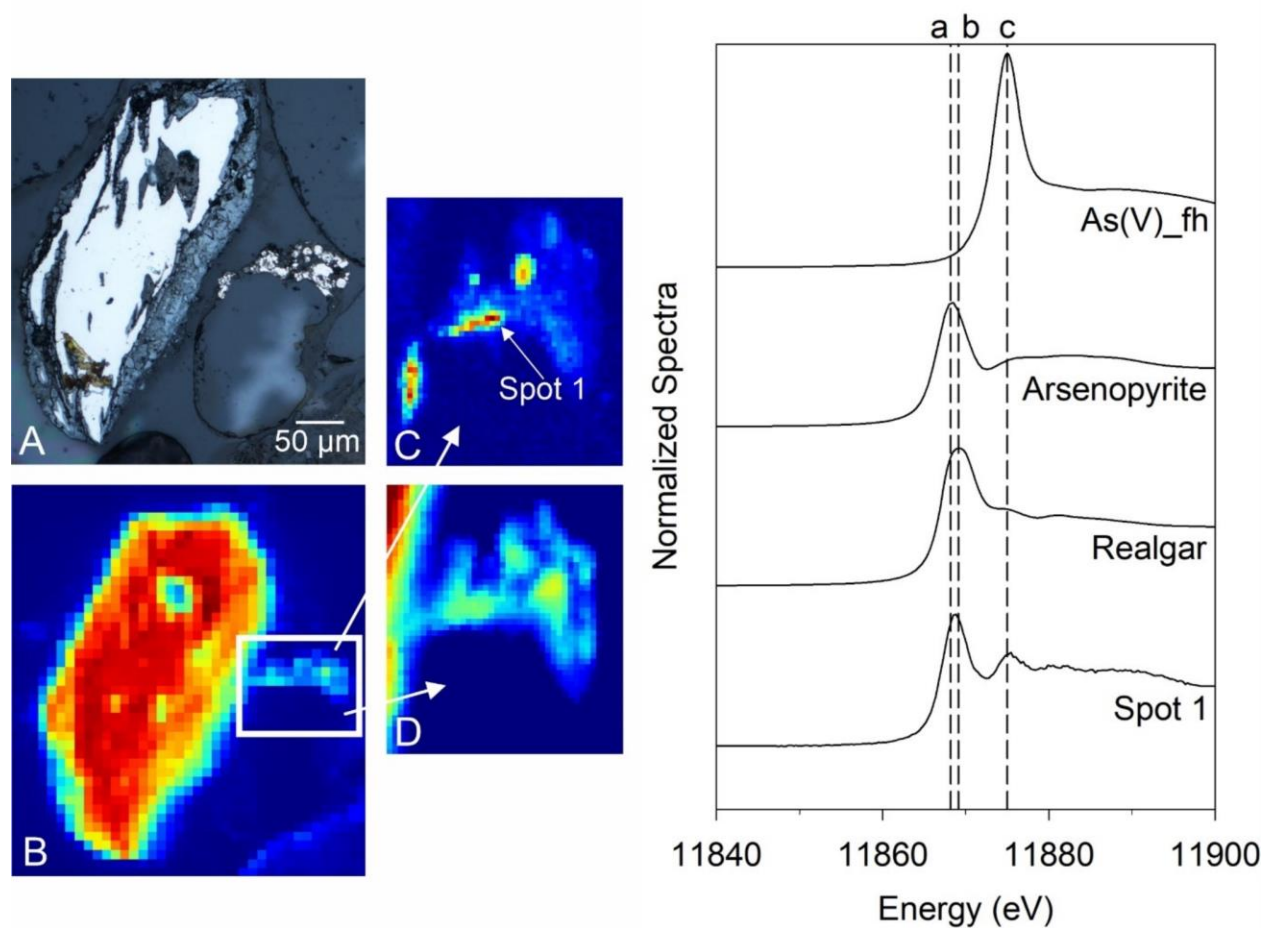


Figure 10. Left: Results from optical microscopy (A), Fe μ XRF imaging (B), and close ups of As μ XRF imaging (C) and Fe μ XRF imaging (D) of a location noted in (B). Right: As μ XANES spectra of a secondary precipitate that formed along the edge of a silica sand grain (column T3). The spectrum collected for spot 1 is plotted with the standards used for LCF. The spectral peak locations of arsenopyrite (a), realgar (b), and As(V) sorbed onto ferrihydrite (c) are shown with dashed lines.

4. Discussion

4.1 Water Chemistry

The high initial pH and alkalinity of the column effluents may be attributed to the dissolution of limestone that was added to the reactive mixture and contributes to the neutralization of acidity through the production of HCO_3^- :



Under anaerobic conditions, the oxidation of OC coupled with SO_4^{2-} reduction is catalyzed by SRB, which also contributes to alkalinity (Waybrant et al., 1998):



where CH_2O represents a simple organic compound. Finally, the anaerobic corrosion of ZVI likely resulted in further neutralization of the pH through the reduction of water and the formation of OH^- (reaction [3]; Blowes et al., 2000; Manning et al., 2002).

An increase in the mean pH in T1, T2, and T3 to 7.3, 7.6, and 7.9, respectively, was consistent with the increase in weight percentage of ZVI in the mixture. All three reactions ([3], [6], [8]) likely contributed to the sharp initial increase in pH and alkalinity and the stable pH values observed throughout the experiments. The addition of Na-lactate, used to stimulate conditions favourable for the growth and activity of SRB, also may have led to increases in the pH and alkalinity at the onset of the experiments.

Decreases in Eh values in all four columns indicate the development of reducing conditions. The presence of OC and ZVI in the reactive mixture likely contributed to a further decrease of Eh values in T1, T2, and T3.

Decreases in Eh, the generation of alkalinity and H₂S, and a decrease in SO₄²⁻ concentrations along the column length of T1, T2, and T3 indicate the development of conditions favourable for SO₄²⁻ reduction at the onset of the experiments. Following the first 5 PVs, the concentrations of H₂S and alkalinity declined (**Figures 1, A6**). The high initial concentrations may be attributed to flushing of the Na-lactate solution present in the columns prior to the introduction of groundwater and to the addition of organic-rich creek sediment.

All of the columns, including the control column, contained organic-rich creek sediment and were initiated with input solution containing lactate and SO₄²⁻. The treatment columns T1, T2, and T3 also contained an organic carbon amendment and ZVI at differing proportions. The addition of these components likely contributed to SO₄²⁻ reduction and generation of H₂S. The presence of ZVI in the reactive mixture likely resulted in the accumulation of FeS precipitates containing Fe derived from the ZVI and S²⁻ derived from sulfate reduction. Unlike the treatment columns, the control column T0 did not contain organic carbon/ZVI amendment. Therefore, the high initial H₂S concentrations in the control column are attributed to activity of SRB utilizing organic carbon from the lactate-containing solution and organic carbon from the sediment amendment. Because the control column T0 did not contain ZVI, the extent of FeS precipitation was lower than in the treatment columns. The formation of sulfide precipitates on the effluent bottle of T0 may also have contributed to the observed changes in the effluent chemistry.

The MPN results suggest the inclusion of OC into the reactive mixture was important for the growth and activity of SRB. Although similar relative abundances of SRB were determined by 16S rRNA sequencing, no culturable SRB were detected in T0, indicating that despite the presence of SRB DNA in the T0 samples, the SRB were not metabolically active. Slightly higher culturable counts of SRB were observed at the influent ends of columns T1, T2, and T3. No

significantly greater ($P > 0.05$) relative abundance of SRB was detected in T1, despite the greatest mass of OC among the three treatment columns. It is possible that bacterial abundance does not increase beyond a threshold mass of OC substrate (the lowest percentage of OC in all three columns was 20 wt. %).

Desulfovibrio was the most abundant SRB genus in columns T1, T2, and T3, whereas *Desulfobulbus* was the most abundant in T0, possibly reflecting differences in overall community structure due to the composition of the column material. *Desulfovibrio* and *Desulfobulbus* members have similar characteristics, including respiratory or fermentative metabolisms, incomplete oxidation of organic compounds, and the ability to use SO_4^{2-} as a terminal electron acceptor to be reduced to H_2S (Kuever et al., 2005). However, organisms within the *Desulfovibrio* genera have been shown to produce more sulfide per unit cell mass utilizing H_2 , compared to lactate, as an electron donor (Steger et al., 2002). The oxidation of ZVI results in the formation of H_2 (reaction [3]) providing a source of H_2 for SRB metabolism. *Desulfovibrio* were more abundant in the treatment columns containing ZVI. Furthermore, *Desulfobulbus* is among the first sulfate-reducing groups to colonize biofilms and, in doing so, could create conditions suitable for other SRB (Acha et al., 2005; Okabe et al., 1999). Therefore, biofilms may have formed on the sand and limestone in T0 in the presence of Na-lactate and organic-rich creek sediment, allowing *Desulfobulbus* to dominate among SRB despite the absence of solid OC added to this column.

Other abundant genera, present in all columns, included *Desulfomicrobium*, *Desulfuromonas*, and *Desulfobacter*. Conditions within the columns fall in the ideal range of pH (6.5-7.5) and temperature (25-35 °C) for the five most abundant SRB genera identified in the column study (Rikihisa et al., 2015). *Desulfovibrio* and *Desulfomicrobium* are both considered important

groups contributing to SO_4^{2-} reduction and As removal in remediation systems (Altun et al., 2014; Omoregie et al., 2013). In addition, some members of *Desulfovibrio* and *Desulfomicrobium* are able to reduce both arsenate and SO_4^{2-} ; a strain of *Desulfomicrobium* may use arsenate as a terminal electron acceptor in the absence of SO_4^{2-} , without affecting SO_4^{2-} reduction (Macy et al., 2000). Some species of the *Desulfuromonas* and *Desulfovibrio* genera also contain a multiheme c-type cytochrome that may function as an Fe(III) reductase, promoting Fe(III) reduction (Macy et al., 2000).

Sulfate concentrations declined with an order of removal of $\text{T1} > \text{T2} = \text{T3} \gg \text{T0}$ for the second SO_4^{2-} concentration profile. The decline in SO_4^{2-} concentrations corresponded to the release of H_2S . The greatest decrease in SO_4^{2-} and increase in H_2S concentrations was observed in column T1, followed by T2 and T3. Lower H_2S values observed toward the middle and end of the experiment were likely due to the precipitation of Fe(II) and other metal sulfides, limiting the aqueous H_2S concentrations. The variable concentrations of H_2S in the first profile may be due to the initial development of microbial populations and the onset of reducing conditions.

Bacteria preferentially utilize ^{32}S in metabolic function relative to the heavier ^{34}S , resulting in enrichment of ^{34}S in the residual SO_4^{2-} (Lindsay et al., 2011a; Nakai and Jensen, 1964; Waybrant et al., 2002). The enrichment in $\delta^{34}\text{S}\text{-SO}_4$ observed in the effluent versus the influent of columns T1, T2, and T3 (**Figure 6**), coupled with the decrease in SO_4^{2-} concentrations, is consistent with the occurrence of bacterially-mediated SO_4^{2-} reduction. The greatest enrichment of $\delta^{34}\text{S}\text{-SO}_4$ (up to 30 ‰) was observed for column T1, which contained the lowest abundance of ZVI. A $\delta^{34}\text{S}\text{-SO}_4$ enrichment factor (ϵ) of -28.9 was calculated for column T1 based on the $\delta^{34}\text{S}\text{-SO}_4$ profile collected at 27 PVs (Clark et al., 2008; Guo and Blowes, 2009). This enrichment factor is within

the range of -20.8 to -46.1 observed in previous experiments utilizing OC to promote SO_4^{2-} reduction (Guo and Blowes, 2009; Lindsay et al., 2009; Waybrant et al., 2002).

Increased alkalinity and H_2S concentrations and decreased Eh were observed in column T0; however, no enrichment of $\delta^{34}\text{S}\text{-SO}_4$ or decrease in SO_4^{2-} concentrations were observed. These differences indicate lower rates of bacterially-mediated SO_4^{2-} reduction in column T0 compared to the other columns. The discrepancy in observed changes to alkalinity, H_2S , and Eh were likely due to sulfide precipitate from the initially added organic-rich creek sediment that accumulated in the effluent bottle. At the end of the experiments, effluent concentrations of SO_4^{2-} in all four columns remained above 40 mg L^{-1} , suggesting SO_4^{2-} reduction was not limited by the availability of SO_4^{2-} during the experiment. If the experiments had continued for longer, the OC source may have become depleted, resulting in an OC-limited system (Waybrant et al., 1998).

4.2 Dissolved Arsenic and Metal Removal

4.2.1 Iron

Iron concentrations remained above the secondary maximum contaminant level of 0.3 mg L^{-1} (EPA) and were up to 50 mg L^{-1} in the column effluents. The increase in Fe along the column length (first profile) at the onset of the experiments may have been due to the development of reducing conditions that resulted in reductive dissolution of Fe (oxy)hydroxide corrosion products on ZVI and creek sediment resulting in Fe mobilization in the early stages of the experiment. The largest increase in Fe concentration was observed in T1, the column with the highest percentage of OC. Over time, the Fe concentrations in all four columns decreased from initial effluent concentrations. The final measured effluent Fe concentration was as low as 2 mg L^{-1} ; suggesting that, with time, Fe concentrations may have decreased further.

Iron-reducing microorganisms (IRM) likely contributed to the higher concentrations of Fe in the effluent. Oxidation of OC can occur by pairing with Fe(III) oxyhydroxides as a terminal electron acceptor (Brock et al., 2006; Lovley & Phillips, 1988):



Iron(II) can be mobilized through bacterially-mediated reduction of Fe (oxy)hydroxides, which may have resulted in the initial increase in Fe concentrations along the column profiles.

Characterization of the microbial community following the termination of the experiment indicated total reads of IRM were low (< 0.1 % of the total microbial reads). However, some SRB genera are capable of directly utilizing Fe(III) as a terminal electron acceptor. The formation of H₂S and subsequent precipitation of Fe sulfides likely resulted in the retention of Fe(II). SEM and optical microscopy confirmed the presence of pyrite, including framboidal pyrite, pyrrhotite, and chalcopyrite. Geochemical modeling indicates the precipitation of other Fe sulfides such as mackinawite ((Fe,Ni)_{1+x}S) and amorphous FeS is favoured (**Figures A.15, A.16**). Geochemical modeling also indicates the potential precipitation of secondary minerals previously observed in reactive barrier studies, including magnetite (Fe₃O₄), maghemite (Fe₂O₃), sphalerite ((Zn, Fe)S), greigite (Fe₃S₄), and amorphous FeS (Gu et al., 1999; Jambor et al., 2005; Lindsay et al., 2008; Rao et al., 2009; **Figures A.17, A.18**).

The formation of pyrite typically proceeds with the formation of disordered mackinawite first (Wolthers et al., 2003), followed by cubic or amorphous FeS, then tetragonal FeS or mackinawite, greigite, and finally marcasite (FeS₂) or pyrite (Jambor et al., 2005). This pathway indicates the importance of mackinawite for the removal of Fe and other metals from the water, and several studies have noted mackinawite is one of the most abundant Fe sulfides present in the reacted material (Gu et al., 1999; Lindsay et al., 2008). The presence of mackinawite and

pyrite, based on the results of geochemical modelling and optical microscopy, indicate Fe was likely removed through the above pathway. Other secondary products such as magnetite and maghemite likely contributed to Fe removal (Gu et al., 1999; Jambor et al., 2005).

Corrosion of ZVI grains, or replacement by secondary precipitates, was observed on grain boundaries and in the form of alteration rims, or on the darkened sections of the grains. Jambor et al. (2005) observed the replacement of ZVI by Fe (oxy)hydroxides as rims and veins around the grain or on the exterior of the grain at sites containing graphite. The Fe (oxy)hydroxides observed in these column experiments are similar in appearance to those observed by Jambor et al. (2005).

Synchrotron-radiation bulk S XANES analysis indicates the accumulation of sulfides on the coatings of the ZVI grain. A comparison between the spectra for the untreated ZVI and the reacted column material shows similar spectral features (c, d) that correspond to tetramethylene sulfoxide (2476 eV) and gypsum (2482 eV) adsorption edges (**Figure 8**). However, “a/b” is absent in the untreated ZVI compared to the column material. This change indicates that, during the experiment, a reduced S phase (pyrite, pyrrhotite, elemental S) accumulated as a coating on the ZVI grains (**Figure 8**). The accumulation of sulfides, including pyrite and pyrrhotite, is consistent with the aqueous, microbiological, and solid phase results that indicate the formation of sulfides through bacterially-mediated SO_4^{2-} reduction. In anoxic environments, the presence of Fe(III) may result in the chemical oxidation of sulfide to S^0 (Lovley & Phillips, 1994; Thamdrup et al., 1993). This process may explain the presence of elemental S in the reactive material. In addition, the S μ XRF and S μ XANES indicate the majority of S present in the secondary precipitates is in reduced phases (pyrite or elemental S). Additional SO_4^{2-} probably accumulated in the column material derived from SO_4^{2-} in the influent water.

The majority of the organic carbon appeared to be unreacted; however, the cellular structure of several particles was replaced by Fe sulfides (**Figure A.12**). SEM analyses indicate the precipitate replacing OC is composed of Fe and S. The μ XRF and S μ XANES results indicate the majority of S present in the secondary precipitate is in the reduced phase, as pyrite or elemental S (**Figure 9**). Replacement of cellular organic matter by sulfides was observed in a similar study, with the sulfide consisting mainly of pyrite and appearing opaque in transmitted light and white under reflected light (Jambor et al., 2005). The formation of secondary carbon is also a common characteristic in sulfate-reducing PRB systems (Jambor et al., 2005).

4.2.2 Arsenic

Influent As concentrations fluctuated during the experiment, which can be divided into four main stages (**Figure 3**). In stage I, As concentrations are low ($24 \mu\text{g L}^{-1}$), probably due to O_2 influx into the bottles during storage. Improved collection methods maintained higher As concentrations in the influent in stage II (4 mg L^{-1} for approximately 10 PVs). In stage III, As concentrations decrease ($103 \mu\text{g L}^{-1}$). Finally, in stage IV, dissolved As and Fe added to the influent solution results in increased concentrations (7.9 mg L^{-1} As, 52.3 mg L^{-1} Fe) for the remainder of the experiment.

The effluent As concentrations in column T0 ranged from 0.3 to 8.3 mg L^{-1} , with a mean of 3.6 mg L^{-1} . Column T0 removed a cumulative mass of 17.8 mg of As, which represents 22.6% removal of the total influent As. In all three treatment columns, effluent As concentrations remained below the EPA maximum contaminant limit of $10 \mu\text{g L}^{-1}$ over the duration of the experiment. Removal occurred within the first 3 cm of reactive material in T1, T2, and T3, with the cumulative masses of As removed (79.6 , 93.4 , and 86.8 mg for T1, T2, and T3, respectively), which represents >99.9% removal of the total influent As.

The reducing conditions that developed within the columns likely contributed to As removal and immobilization due to two reactions. First, the formation of H₂S through bacterially-mediated SO₄²⁻ reduction may have resulted in the precipitation of As-bearing secondary sulfide minerals (reactions [4] and [5]; Blowes et al., 2000; Jambor et al., 2005). High concentrations of H₂S at the onset of the experiment, followed by lower concentrations, reflect removal through metal sulfide precipitation. Synchrotron results also indicate the presence of As in secondary precipitates containing Fe and S. Second, the ZVI in the mixture and the formation of Fe (oxy)hydroxides and secondary sulfide precipitates (reaction [3]) likely created surfaces suitable for As adsorption. Synchrotron results indicate the presence of sorbed arsenate onto ferrihydrite on secondary precipitates. Retention of As may be due to mechanisms such as incorporation into the tetrahedral Fe-S layers of mackinawite or adsorption onto Fe oxyhydroxides (Bowell, 1994; Mullet et al., 2002). Water samples from profile measurements were undersaturated with respect to crystalline As-bearing phases including realgar and orpiment. However, As concentrations in the treatment column profiles declined sharply upstream from to the first sampling port; for example, in the second profile (27 PVs) for column T1 the As concentration declined from 8.9 mg L⁻¹ to < 5 µg L⁻¹ upstream from port 1, suggesting any removal of As by sulfide precipitation occurred upstream from the first sampling port. Iron corrosion products including maghemite, magnetite, hematite (Fe₂O₃), and goethite (FeO(OH)) may have affected the ZVI and As interaction and also contributed to the rapid removal of As (Rao et al., 2009; Su and Puls, 2001). Arsenic may have been removed through co-precipitation with Fe sulfides or incorporation by inner-sphere adsorption onto the surface of goethite and other FeOOH polymorphs (Ludwig et al., 2009; Stichbury, 2000).

Synchrotron-radiation based μ XRF and μ XANES results indicate the presence of As in the secondary precipitates, which contain Fe and S and surround grains of silica sand (**Figures 10, A.14**). The μ XANES spectral features associated with As(V) are most similar to arsenate sorbed to ferrihydrite. Reduced As phases, including realgar, orpiment, and arsenopyrite, were also observed. Kankite may also occur within the secondary product replacing cellular organic material. These observations indicate As is likely incorporated into the structure of secondary precipitates through sorption or co-precipitation. A combination of μ XANES/ μ XRF results indicate the formation of As-sulfide minerals occurs, despite geochemical modelling results indicating undersaturation with respect to realgar and orpiment. As noted above, the majority of these minerals likely formed upstream from the first sampling port. Both reduced and oxidized forms of As are present in the secondary precipitates; however, the majority of As is in the reduced form (-1, +3). Reduced As is anticipated to be present due to the reducing conditions that were sustained within the column. In addition, the reducing and anoxic conditions maintained throughout the experiment suggest the As immobilized in the sulfide form should be geochemically stable.

4.2.3 Other Transition Met

A sharp decrease in metal concentrations was observed between the influent and effluent (Al, Cd, Co, Cu, Ni, Zn; **Figure 5**). The increase in pH and the precipitation of secondary Al (oxy)hydroxides, including gibbsite (γ -Al(OH)₃) and boehmite (γ -AlO(OH)), likely contributed to the removal of Al (**Figure A.15**). The presence of higher concentrations of H₂S early in the experiment further suggests the decline in metal concentrations is due to the precipitation of low-solubility metal sulfides (reactions [4] and [5]). In the presence of dissolved Fe(II) and H₂S, disordered mackinawite is predicted to be the first phase to precipitate (Wolthers et al., 2003).

Geochemical modeling indicates the water is saturated with respect to sulfide minerals such as sphalerite, chalcopyrite, covellite (CuS), and chalcocite (Cu₂S; **Figure A.16**); this suggests the formation of these sulfide minerals, or less crystalline precursors, likely contributed to the removal of Cu and Zn. Retention of metals may be due to incorporation into the tetrahedral Fe-S layers of mackinawite (Mullet et al., 2002). In addition, adsorption onto organic matter and other (co)precipitated phases such as Fe and Al (oxy)hydroxides may also contribute to retention of metals (Gibert et al., 2005). The removal and retention of metals including Cu, Zn, and Ni are likely due to the formation of low-solubility metal sulfides and adsorption onto Fe sulfides and Fe (oxy)hydroxides.

4.3 Carbon and Nutrient Release

The initial release of NH₃-N and PO₄-P in T1, T2, and T3 could be due to the breakdown of organic matter containing N and P (Paulson et al., 2018; Waybrant et al., 2002). Decomposition of organic material likely promoted the growth of heterotrophic SRB that utilize SO₄²⁻ as an electron acceptor (Herbert Jr et al., 2000). Although column T1 contained the highest OC content, the concentrations of PO₄-P and NH₃-N were similar to columns T2 and T3; PO₄-P and NH₃-N were lower in column T0 (**Figure A.6**). Despite high effluent concentrations of NH₃-N and PO₄-P early in the experiments, an overall decrease in concentrations occurred over time. PO₄-P and NH₃-N concentrations persisted in the porewater in later stages of the experiment (**Figure A.6**).

High DOC concentrations observed at the onset of the experiment are attributed to the initial flush of groundwater through the OC present in the reactive material (Lindsay et al., 2011a). The initial increase could be due to two reasons. First, Na-lactate solution and residual carbon, added as creek sediment, was likely broken down and released during the first few PVs. Second, the

initial surge could be attributed to the rapid depletion of labile organic carbon from the initial labile OC present in the reactive mixture. Following depletion of this initial labile OC, *in situ* OC degradation may have become the main source of OC available for bacterially-mediated SO_4^{2-} reduction (Lindsay et al., 2011a). Organic carbon may also be utilized as an electron donor for Fe reduction (reactions [4] and [5]), suggesting the high initial DOC concentrations may have contributed to an increase in Fe concentrations. The high initial DOC concentrations observed in T0 are also attributed to the Na-lactate and residual carbon, despite minimal OC in the column mixture. The slight increase in DOC along the length of T0 at 47 PVs, may be due to residual carbon remaining from the initial organic-rich creek sediment added during packing. However, overall effluent DOC concentrations in T0 were below 10 mg L^{-1} following the initial surge, remaining at concentrations lower than the effluent concentrations of the three reactive columns (T1, T2, T3). Increases in DIC concentrations were also observed in all four columns. The largest increase in DIC was observed in column T1, corresponding to the highest percentage of OC in the reactive mixture. DIC concentrations may increase due to mineralization of organic matter coupled with bacterially-mediated SO_4^{2-} reduction (Asmussen and Strauch, 1998).

An enrichment in $\delta^{13}\text{C}$ -DIC at the first sampling port was followed by a gradual decrease in $\delta^{13}\text{C}$ -DIC along the length of columns T1, T2, and T3 (**Figure 6**). In column T0, following the initial enrichment, the $\delta^{13}\text{C}$ -DIC values remained relatively constant at near 0 ‰ for the remainder of the column length; this trend reflects the influence of limestone from the reactive material. The slight increase in alkalinity within the first 3 cm of reactive material corresponds to a sharp increase in $\delta^{13}\text{C}$ -DIC values. Column T3, with the lowest percentage of OC in the reactive mixture, showed the sharpest increase in $\delta^{13}\text{C}$ -DIC, followed by T2 and then T1. Despite the increase in $\delta^{13}\text{C}$ -DIC ratios, values remained relatively depleted, especially in columns T1

(-14.8 ‰) and T2 (-15.1 ‰). Minimal depletion of $\delta^{13}\text{C}$ -DIC was observed in column T0, with values remaining near 0 ‰ along the column length due to the limited influence of OC in the column mixture. The enrichment of $\delta^{34}\text{S}$ - SO_4 combined with the depletion of $\delta^{13}\text{C}$ -DIC is indicative of SO_4^{2-} reduction coupled with oxidation of organic carbon. A slight decrease in $\delta^{13}\text{C}$ -DIC was observed along the column length. The lower ratios observed in T1 may be attributed to a contribution from labile OC (leaf mulch and wood chips).

4.4 Sulfate Reaction Rates

The removal rates of SO_4^{2-} in the treatment columns were calculated based on the second profiles collected from columns T1, T2, and T3 at 27, 40, and 38 PVs, respectively (**Figure A.19**).

Sulfate removal rates within all three columns are consistent with a zero-order rate equation, $C = -k_0t$, where C is the SO_4^{2-} concentration (mg L^{-1}), t is the residence time (d), and k_0 is the zero-order rate constant for SO_4^{2-} removal ($\text{mg L}^{-1} \text{d}^{-1}$). The three treatment columns had similar SO_4^{2-} removal rates, with $R_{S,1} = -33.10 \text{ mg L}^{-1} \text{d}^{-1}$ for T1, $R_{S,2} = -33.13 \text{ mg L}^{-1} \text{d}^{-1}$ for T2, and $R_{S,3} = -30.39 \text{ mg L}^{-1} \text{d}^{-1}$ for T3. The negative rate constants indicate SO_4^{2-} was removed. The zero-order rate expression provides a reasonable description for the rate of SO_4^{2-} reduction ($R^2 > 0.93$). The weight percentage of dry OC varied in each of the three treatment columns from 20 to 40 wt. %. The normalized SO_4^{2-} removal rates were -0.18 (T1), -0.18 (T2), and $-0.20 \text{ mg L}^{-1} \text{d}^{-1} \text{g}^{-1}$ of dry OC (T3).

The influence of ZVI on the SO_4^{2-} removal rates for the three treatment columns appears to be minimal, as observed in the similarity between normalized rates. The rates indicate that above 10 wt. % ZVI, there may be minimal influence to the overall reactive mixture. Additional tests utilizing mixtures with less than 10 wt. % ZVI may be beneficial to an increased understanding of the minimum wt % ZVI required to remove metal(oids) and SO_4^{2-} from the water. Mixtures

with lower percentages of ZVI may also release lower concentrations of Fe in the initial flushing of groundwater through the mixture.

The zero-order equation for reaction rates has been used in similar studies (Benner et al., 2002). Reported rates vary from -0.14 to $-4.23 \text{ mg L}^{-1} \text{ d}^{-1} \text{ g}^{-1}$ of dry OC (Waybrant et al., 2002) to -1.24 to $-1.40 \text{ } \mu\text{g L}^{-1} \text{ d}^{-1} \text{ g}^{-1}$ of dry OC (Lindsay et al., 2008) in studies utilizing similar material. The bulk SO_4^{2-} removal rate for a field barrier system (Benner et al., 2002), was between 40 and 58 $\text{mmol L}^{-1} \text{ a}^{-1}$ (10.5 - $15.3 \text{ mg L}^{-1} \text{ d}^{-1}$), which is of similar magnitude to the rates observed in our study (Benner et al., 2002). Sulfate reduction rates were very similar to a laboratory system containing only OC (Waybrant et al., 2002). The removal rate observed in our system was approximately two orders of magnitude higher than a study containing both OC and ZVI and that determined SO_4^{2-} removal rates using a mass-based approach rather than an aqueous concentration-based method (Lindsay et al., 2008). Variances in the reactive material used may also have affected SO_4^{2-} reduction rates. Mixtures varied from those containing only organic carbon (Benner et al., 2002; Waybrant et al., 2002) to those that included ZVI (Lindsay et al., 2008).

Similar SO_4^{2-} removal rates were observed in all three treatment columns (T1, T2, T3). In a similar experiment, a higher removal rate was observed in a mixture containing 50 vs. 40 dry wt. % OC in a microcosm study (Lindsay et al., 2008). Even though the addition of OC has been shown to enhance SO_4^{2-} reduction rates, a substantial enhancement in reaction rates may not occur above a certain dry wt. % of OC (Lindsay et al., 2008). Based on the similar rates calculated for all three of our treatment columns, the SO_4^{2-} reaction rate may not be further enhanced at OC contents above 20 wt. % (the lowest percentage of OC considered). However, the abundance of OC may affect the longevity of the reactive mixture (Lindsay et al., 2008).

4.5 Long-term Capacity

The long-term potential of the reactive mixture may be influenced by both biotic and abiotic factors. Abiotic factors, including corrosion of ZVI, may result in declining reactivity and clogging of the reactive material by secondary precipitates, which may reduce the porosity and limit the reactive surface area (Henderson & Demond, 2007). Biotic factors, greatly influenced by the availability of OC, also affect the long-term effectiveness of the reactive material. Limited labile OC can negatively affect the growth and activity of heterotrophic microbial communities and decrease the rate of SO_4^{2-} reduction. A recent study evaluated the injection of emulsified vegetable oil (EVO) as an additional source of carbon to enhance reactivity of a PRB system (Legrand et al., 2016). Loss of permeability and reactivity of the material were not observed in this study, but should be considered when evaluating the long-term potential of the reactive material.

5. Conclusions

Removal of As, metals, and SO_4^{2-} was observed in all treatment columns. The pH of the groundwater increased from to $\text{pH} < 4$ to circumneutral values before the first sampling port, and a $\text{pH} > 7$ was maintained throughout the experiment. The onset of reducing conditions and bacterially-mediated SO_4^{2-} reduction resulted in decreases in SO_4^{2-} concentrations, H_2S production, enrichment of $\delta^{34}\text{S}\text{-SO}_4$, and the presence of SRB populations in all treatment columns. Column T0, containing minimal amounts of OC, removed metals from the groundwater, but did not contain sufficient OC to sustain sulfate-reducing conditions and result in As removal. A higher relative abundance of SRB was observed at the influent vs. effluent end of the treatment columns. Above 20 wt. % OC, no additional increase in SRB abundance or

activity was observed. Sulfate removal rates ranged from 0.18 to 0.20 mg L⁻¹ d⁻¹ g⁻¹ dry OC for the three treatment columns. Removal rates were within one order of magnitude of previous laboratory column experiments utilizing similar reactive material. Varying the wt. % of ZVI and OC resulted in modest changes to SO₄²⁻ removal rates.

Results from synchrotron radiation bulk S XANES indicate the accumulation of reduced S phases, including pyrite and FeS, on ZVI grain coatings. Removal of Fe and other metals is attributed to bacterially-mediated SO₄²⁻ reduction and the subsequent precipitation of low solubility metal sulfides including pyrite, sphalerite, chalcopyrite, or less-crystalline precursors. Removal of Fe may also be due to the replacement of cellular organic material by an Fe-sulfide precipitate. A decrease in effluent Fe concentrations was observed over time, but concentrations remained above 2 mg L⁻¹ throughout the experiment.

The removal of As is attributed to adsorption onto Fe (oxy)hydroxides and precipitation of As-bearing secondary sulfide minerals. Arsenic is present as both oxidized and reduced species in the form of secondary precipitates and adsorbed products. Arsenite is immobilized as As-crystalline phases including realgar and orpiment, and arsenate is removed through adsorption onto ferrihydrite. The reducing and anoxic conditions of the column material indicate that immobilized As should be geochemically stable.

This study demonstrates the potential for the reactive material, which contains a mixture of OC, ZVI, and limestone, to remove metal(loids) from acidic groundwater. No significant difference among the three treatment columns was observed, suggesting a cost-effective composition of reactive material may utilize minimal ZVI (10 wt. %). Further evaluation of the reactive material is needed to determine the long-term capabilities of the mixture. In addition, evaluation of the

material under field conditions would increase our understanding of the influence of changing temperatures on the reactivity of the column material.

Acknowledgements

This work was supported by the Natural Sciences and Engineering Research Council of Canada, TERRE-NET (Grant Number: NETGP 479708-15) and the Ministry of Energy, Northern Development and Mines (ENDM). Synchrotron-based techniques were performed at Sector 20-ID of the Advanced Photon Source, a U.S. Department of Energy (DOE) Office of Science User Facility operated for the DOE Office of Science by Argonne National Laboratory under Contract No. DE-AC02-06CH11357. Additional synchrotron-based techniques were performed using beamline SXRMB at the Canadian Light Source, a national research facility of the University of Saskatchewan, which is supported by the Canada Foundation for Innovation (CFI), the Natural Sciences and Engineering Research Council (NSERC), the National Research Council (NRC), the Canadian Institutes of Health Research (CIHR), the Government of Saskatchewan, and the University of Saskatchewan.

References

- Achá, D., Iñiguez, V., Roulet, M., Remy, J., Guimarães, D., Luna, R., Alanoca, L., & Sanchez, S. (2005). Sulfate-reducing bacteria in floating macrophyte rhizospheres from an amazonian floodplain lake in Bolivia and their association with Hg methylation. *Applied and Environmental Microbiology*, 71(11), 7531–7535. <https://doi.org/10.1128/AEM.71.11.7531-7535.2005>
- Altun, M., Sahinkaya, E., Durukan, I., Bektas, S., & Komnitsas, K. (2014). Arsenic removal in a

- sulfidogenic fixed-bed column bioreactor. *Journal of Hazardous Materials*, 269, 31–37.
<https://doi.org/10.1016/j.jhazmat.2013.11.047>
- Asmussen, G., & Strauch, G. (1998). Sulfate reduction in a lake and the groundwater of a former lignite mining area studied by stable sulfur and carbon isotopes. *Water, Air, and Soil Pollution*, 108(3–4), 271–284.
- Bain, J., Spink, L., Blowes, D. W., & Smyth, D. (2002). The removal of arsenic from groundwater using permeable reactive materials. *9th International Conference on Tailings and Mine Waste*, 213–216.
- Ball, J. W., & Nordstrom, D. K. (1991). User's manual for WATEQ4F, with revised thermodynamic data base and test cases for calculating speciation of major, trace, and redox elements in natural waters. *U.S. Geological Survey*. <https://doi.org/10.3133/ofr91183>
- Bang, S., Korfiatis, G. P., & Meng, X. (2005). Removal of arsenic from water by zero-valent iron. *Journal of Hazardous Materials*, 121(1–3), 61–67. <https://doi.org/10.1016/j.jhazmat.2005.01.030>
- Benner, S. G., Blowes, D. W., Gould, W. D., Herbert Jr., R. B., & Ptacek, C. J. (1999). Geochemistry of a permeable reactive barrier for metals and acid mine drainage. *Environmental Science and Technology*, 33(16), 2793–2799. <https://doi.org/10.1021/es981040u>
- Benner, S. G., Blowes, D. W., & Ptacek, C. J. (1997). A full-scale porous reactive wall for prevention of acid mine drainage. *Groundwater Monitoring and Remediation*, 17(4), 99–107.
- Benner, S. G., Blowes, D. W., Ptacek, C. J., & Mayer, K. U. (2002). Rates of sulfate reduction and metal sulfide precipitation in a permeable reactive barrier. *Applied Geochemistry*, 17(3), 301–320.
[https://doi.org/10.1016/S0883-2927\(01\)00084-1](https://doi.org/10.1016/S0883-2927(01)00084-1)
- Biterna, M., Antonoglou, L., Lazou, E., & Voutsas, D. (2010). Arsenite removal from waters by zero valent iron: Batch and column tests. *Chemosphere*, 78(1), 7–12.
<https://doi.org/10.1016/j.chemosphere.2009.10.007>

- Biterna, M., Arditoglou, A., Tsikouras, E., & Voutsas, D. (2007). Arsenate removal by zero valent iron: Batch and column tests. *Journal of Hazardous Materials*, 149(3), 548–552.
<https://doi.org/10.1016/j.jhazmat.2007.06.084>
- Blowes, D. W., & Jambor, J. L. (1990). The pore-water geochemistry and the mineralogy of the vadose zone. *Applied Geochemistry*, 5, 327–346. [https://doi.org/10.1016/0883-2927\(90\)90008-S](https://doi.org/10.1016/0883-2927(90)90008-S)
- Blowes, D. W., Ptacek, C. J., Benner, S. G., McRae, C. W. T., Bennett, T. A., & Puls, R. W. (2000). Treatment of inorganic contaminants using permeable reactive barriers. *Journal of Contaminant Hydrology*, 45(1–2), 123–137. [https://doi.org/10.1016/S0169-7722\(00\)00122-4](https://doi.org/10.1016/S0169-7722(00)00122-4)
- Blowes, D. W., Ptacek, C. J., Benner, S. G., Waybrant, K. R., & Bain, J. G. (1998). Porous reactive walls for the prevention of acid mine drainage: a review. *Mineral Processing and Extractive Metallurgy Review*, 19(1), 25–37. <https://doi.org/10.1080/08827509608962426>
- Blowes, D. W., Ptacek, C. J., Jambor, J. L., Weisener, C. G., Paktunc, D., Gould, W. D., & Johnson, D. B. (2014). The geochemistry of acid mine drainage. In H. D. Holland & K. K. Turekian (Eds.), *Treatise on Geochemistry: Second Edition* (Vol. 11). Elsevier Science.
<https://doi.org/10.1016/B978-0-08-095975-7.00905-0>
- Bowell, R. J. (1994). Sorption of arsenic by iron oxides and oxyhydroxides in soils. *Applied Geochemistry*, 9, 279–286. [https://doi.org/10.1016/0883-2927\(94\)90038-8](https://doi.org/10.1016/0883-2927(94)90038-8)
- Brock, F., Parkes, R. J., & Briggs, D. E. G. (2006). Experimental pyrite formation associated with decay of plant material. *Palaios*, 21(5), 499–506. <https://doi.org/10.2110/palo.2005.p05-077r>
- CH2MHill. (2014). *Site Characterization Report and Data Analysis – Long Lake Gold Mine Tailings Areas, Eden Township, Ontario*.
- Clark, S. K., & Johnson, T. M. (2008). Effective isotopic fractionation factors for solute removal by reactive sediments: A laboratory microcosm and slurry study. *Environmental Science and*

- Technology*, 42(21), 7850–7855. <https://doi.org/10.1021/es801814v>
- Cochran, W. G. (1950). Estimation of bacterial densities by means of the “most probable number.” *Biometrics*, 6(2), 105–116. <https://www.jstor.org/stable/3001491>
- Evangelou, V. P., & Zhang, Y. L. (1995). A review: Pyrite oxidation mechanisms and acid mine drainage prevention. *Critical Reviews in Environmental Science and Technology*, 25(2), 141–199. <https://doi.org/10.1080/10643389509388477>
- Fleet, M. E. (2005). XANES spectroscopy of sulfur in earth materials. *The Canadian Mineralogist*, 43(6), 1811–1838.
- Foster, A. L., & Kim, C. S. (2014). Arsenic speciation in solids using X-ray absorption spectroscopy. *Reviews in Mineralogy & Geochemistry*, 79, 257–369. <https://doi.org/10.2138/rmg.2014.79.5>
- Gibert, O., De Pablo, J., Cortina, J. L., & Ayora, C. (2005). Municipal compost-based mixture for acid mine drainage bioremediation: Metal retention mechanisms. *Applied Geochemistry*, 20(9), 1648–1657. <https://doi.org/10.1016/j.apgeochem.2005.04.012>
- Gould, J. P. (1982). The kinetics of hexavalent chromium reduction by metallic iron. *Water Research*, 16(6), 871–877. [https://doi.org/10.1016/0043-1354\(82\)90016-1](https://doi.org/10.1016/0043-1354(82)90016-1)
- Gould, W. D., Stichbury, M., Francis, M., Lortie, L., & Blowes, D. W. (2003). An MPN method for enumeration of iron-reducing bacteria. *Mining and the Environment Conference*.
- Gu, B., Phelps, T. J., Liang, L., Dickey, M. J., Roh, Y., Kinsall, B. L., Palumbo, A. V., & Jacobs, G. K. (1999). Biogeochemical dynamics in zero-valent iron columns: Implications for permeable reactive barriers. *Environmental Science and Technology*, 33(13), 2170–2177. <https://doi.org/10.1021/es981077e>
- Guo, Q., & Blowes, D. W. (2009). Biogeochemistry of two types of permeable reactive barriers, organic carbon and iron-bearing organic carbon for mine drainage treatment: Column experiments. *Journal*

- of Contaminant Hydrology*, 107(3–4), 128–139. <https://doi.org/10.1016/j.jconhyd.2009.04.008>
- Henderson, A. D., & Demond, A. H. (2007). Review long-term performance of zero-valent iron permeable reactive barriers: a critical review. *Environmental Engineering Science*, 24(4), 401–423. <https://doi.org/10.1089/ees.2006.0071>
- Herbert Jr, R. B., Benner, S. G., & Blowes, D. W. (2000). Solid phase iron-sulfur geochemistry of a reactive barrier for treatment of mine drainage. *Applied Geochemistry*, 15(9), 1331–1343. [https://doi.org/10.1016/S0883-2927\(00\)00005-6](https://doi.org/10.1016/S0883-2927(00)00005-6)
- Jambor, J. L., Raudsepp, M., & Mountjoy, K. (2005). Mineralogy of permeable reactive barriers for the attenuation of subsurface contaminants. *Canadian Mineralogist*, 43(6), 2117–2140. <https://doi.org/10.2113/gscanmin.43.6.2117>
- Jeen, S. W., Bain, J. G., & Blowes, D. W. (2014). Evaluation of mixtures of peat, zero-valent iron and alkalinity amendments for treatment of acid rock drainage. *Applied Geochemistry*, 43, 66–79. <https://doi.org/10.1016/j.apgeochem.2014.02.004>
- Jeen, S. W., Jambor, J. L., Blowes, D. W., & Gillham, R. W. (2007). Precipitates on granular iron in solutions containing calcium carbonate with trichloroethene and hexavalent chromium. *Environmental Science and Technology*, 41(6), 1989–1994. <https://doi.org/10.1021/es0618393>
- Kozich, J. J., Westcott, S. L., Baxter, N. T., Highlander, S. K., & Schloss, P. D. (2013). Development of a Dual-Index Sequencing Strategy and Curation Pipeline for Analyzing Amplicon Sequence Data on the MiSeq Illumina Sequencing Platform. *Applied and Environmental Microbiology*, 79(17), 5112–5120. <https://doi.org/10.1128/AEM.01043-13>
- Kuever, J., Rainey, F. A., & Widdel, F. (2005). Class IV. Deltaproteobacteria class nov. In D. J. Brenner, N. R. Krieg, & J. T. Staley (Eds.), *Bergey's Manual® of Systematic Bacteriology: Volume Two The Proteobacteria Part C The Alpha-, Beta-, Delta-, and Epsilonproteobacteria* (pp. 922–1144).

Springer US. https://doi.org/10.1007/978-0-387-29298-4_3

- Legrand, R., Maestas, K. M., Henry, R. L., Bain, J. G., Blowes, D. W., Strunk, J. F., & Chai, Y. (2016). Pilot testing of a permeable reactive barrier (PRB) to remediate sulfate, metals, and low Ph in groundwater. *2016 SME Annual Conference and Expo: The Future for Mining in a Data-Driven World*, 723–728.
- Lien, H. L., & Wilkin, R. T. (2005). High-level arsenite removal from groundwater by zero-valent iron. *Chemosphere*, 59(3), 377–386. <https://doi.org/10.1016/j.chemosphere.2004.10.055>
- Lindsay, M. B. J., Blowes, D. W., Condon, P. D., & Ptacek, C. J. (2009). Managing pore-water quality in mine tailings by inducing microbial sulfate reduction. *Environmental Science and Technology*, 43(18), 7086–7091. <https://doi.org/10.1021/es901524z>
- Lindsay, M. B. J., Blowes, D. W., Condon, P. D., & Ptacek, C. J. (2011). Organic carbon amendments for passive in situ treatment of mine drainage: Field experiments. *Applied Geochemistry*, 26(70), 1169–1183. <https://doi.org/10.1016/j.apgeochem.2011.04.006>
- Lindsay, M. B. J., Blowes, D. W., Ptacek, C. J., & Condon, P. D. (2011). Transport and attenuation of metal(loid)s in mine tailings amended with organic carbon: Column experiments. *Journal of Contaminant Hydrology*, 125(1–4), 26–38. <https://doi.org/10.1016/j.jconhyd.2011.04.004>
- Lindsay, M. B. J., Ptacek, C. J., Blowes, D. W., & Gould, W. D. (2008). Zero-valent iron and organic carbon mixtures for remediation of acid mine drainage: Batch experiments. *Applied Geochemistry*, 23(8), 2214–2225. <https://doi.org/10.1016/j.apgeochem.2008.03.005>
- Liu, Y. Y., Ptacek, C. J., & Blowes, D. W. (2014). Treatment of dissolved perchlorate, nitrate, and sulfate using zero-valent iron and organic carbon. *Journal of Environmental Quality*, 43(3), 842–850. <https://doi.org/10.2134/jeq2013.03.0077>
- Lovley, D. R., & Phillips, E. J. P. (1988). Novel mode of microbial energy metabolism: organic carbon

- oxidation coupled to dissimilatory reduction of iron or manganese. *Applied and Environmental Microbiology*, 54(6), 1472–1480. <http://aem.asm.org/>
- Lovley, D. R., & Phillips, E. J. P. (1994). Novel processes for anaerobic sulfate production from elemental sulfur by sulfate-reducing bacteria. *Applied and Environmental Microbiology*, 60(7), 2394–2399. <http://aem.asm.org/>
- Ludwig, R. D., McGregor, R. G., Blowes, D. W., Benner, S. G., & Mountjoy, K. (2002). A permeable reactive barrier for treatment of heavy metals. *Ground Water*, 40(1), 59–66. <https://doi.org/10.1111/j.1745-6584.2002.tb02491.x>
- Ludwig, R. D., Smyth, D. J. A., Blowes, D. W., Spink, L. E., Wilkin, R. T., Jewett, D. G., & Weisener, C. J. (2009). Treatment of arsenic, heavy metals, and acidity using a mixed ZVI-compost PRB. *Environmental Science and Technology*, 43(6), 1970–1976. <https://doi.org/10.1021/es802394p>
- Macy, J. M., Santini, J. M., Pauling, B. V., O'Neill, A. H., & Sly, L. I. (2000). Two new arsenate/sulfate-reducing bacteria: mechanisms of arsenate reduction. *Archives of Microbiology*, 173(1), 49–57. <https://doi.org/10.1007/s002030050007>
- Manning, B., Hunt, M., Amrhein, C., & Yarmoff, J. (2002). Arsenic(III) and arsenic(V) reactions with zerovalent iron corrosion products. *Environmental Science and Technology*, 36(24), 5455–5461. <https://doi.org/10.1021/es0206846>
- Moncur, M. C., Ptacek, C. J., Blowes, D. W., & Jambor, J. L. (2005). Release, transport and attenuation of metals from an old tailings impoundment. *Applied Geochemistry*, 20(3), 639–659. <https://doi.org/10.1016/j.apgeochem.2004.09.019>
- Mullet, M., Boursiquot, S., Abdelmoula, M., Génin, J. M., & Ehrhardt, J. J. (2002). Surface chemistry and structural properties of mackinawite prepared by reaction of sulfide ions with metallic iron. *Geochimica et Cosmochimica Acta*, 66(5), 829–836. [https://doi.org/10.1016/S0016-7037\(01\)00805-](https://doi.org/10.1016/S0016-7037(01)00805-)

- Nakai, N., & Jensen, M. L. (1964). The kinetic isotope effect in the bacterial reduction and oxidation of sulfur. *Geochimica et Cosmochimica Acta*, 28(12), 1893–1912. [https://doi.org/10.1016/0016-7037\(64\)90136-X](https://doi.org/10.1016/0016-7037(64)90136-X)
- Okabe, S., Itoh, T., Satoh, H., & Watanabe, Y. (1999). Analyses of spatial distributions of sulfate-reducing bacteria and their activity in aerobic wastewater biofilms. *Applied and Environmental Microbiology*, 65(11), 5107–5116. <https://doi.org/10.1128/AEM.65.11.5107-5116.1999>
- Omeregic, E. O., Couture, R.-M., Cappellen, P. Van, Corkhill, C. L., Charnock, J. M., Polya, D. A., Vaughan, D., Vanbroekhoven, K., & Lloyd, J. R. (2013). Arsenic bioremediation by biogenic iron oxides and sulfides. *Applied and Environmental Microbiology*, 79(14), 4325–4335. <https://doi.org/10.1128/AEM.00683-13>
- Pagnanelli, F., Cruz Viggì, C., Mainelli, S., & Toro, L. (2009). Assessment of solid reactive mixtures for the development of biological permeable reactive barriers. *Journal of Hazardous Materials*, 170(2–3), 998–1005. <https://doi.org/10.1016/j.jhazmat.2009.05.081>
- Pakostova, E., Schmall, A. J., Holland, S. P., White, H., Ptacek, C. J., & Blowes, D. W. (2020). Performance of a geosynthetic-clay-liner cover system at a Cu/Zn mine tailings impoundment. *Applied and Environmental Microbiology*, 86(8). <https://doi.org/10.1128/AEM.02846-19>
- Paulson, K. M. A., Ptacek, C. J., Blowes, D. W., Gould, W. D., Ma, J., Landis, R. C., & Dyer, J. A. (2018). Role of organic carbon sources and sulfate in controlling net methylmercury production in riverbank sediments of the South River, VA (USA). *Geomicrobiology Journal*, 35(1), 1–14. <https://doi.org/10.1080/01490451.2016.1247483>
- Postgate, J. R. (1984). *The Sulphate-Reducing Bacteria*, 2nd Ed. Cambridge University Press, Cambridge.
- Rao, P., Mak, M. S. H., Liu, T., Lai, K. C. K., & Lo, I. M. C. (2009). Effects of humic acid on arsenic(V)

- removal by zero-valent iron from groundwater with special references to corrosion products analyses. *Chemosphere*, 75(2), 156–162. <https://doi.org/10.1016/j.chemosphere.2008.12.019>
- Ravel, B., & Newville, M. (2005). Synchrotron radiation ATHENA, ARTEMIS, HEPHAESTUS: data analysis for X-ray absorption spectroscopy using IFEFFIT. *Journal of Synchrotron Radiation*, 12, 537–541. <https://doi.org/10.1107/S0909049505012719>
- Rikihisa, Y., Stephen Dumler, J., & Dasch, G. A. (2015). *Bergey's Manual of Systematics Bacteriology*. <https://doi.org/10.1002/9781118960608.gbm00905>
- Schloss, P. D., Westcott, S. L., Ryabin, T., Hall, J. R., Hartmann, M., Hollister, E. B., Lesniewski, R. A., Oakley, B. B., Parks, D. H., Robinson, C. J., Sahl, J. W., Stres, B., Thallinger, G. G., Van Horn, D. J., & Weber, C. F. (2009). Introducing mothur: Open-Source, Platform-Independent, Community-Supported Software for Describing and Comparing Microbial Communities. *Applied and Environmental Microbiology*, 75(23), 7537–7541. <https://doi.org/10.1128/AEM.01541-09>
- Sprague, D. D., Michel, F. A., & Vermaire, J. C. (2016). The effects of migration on ca. 100-year-old arsenic-rich mine tailings in Cobalt, Ontario, Canada. *Environmental Earth Sciences*, 75(5), 1–12. <https://doi.org/10.1007/s12665-015-4898-1>
- Steger, J. L., Vincent, C., Ballard, J. D., & Krumholz, L. R. (2002). Desulfovibrio sp. Genes Involved in the Respiration of Sulfate during Metabolism of Hydrogen and Lactate Downloaded from. *Applied and Environmental Microbiology*, 68(4), 1932–1937. <https://doi.org/10.1128/AEM.68.4.1932-1937.2002>
- Stichbury, M. K. (2000). *Mechanisms of Release and Attenuation of Arsenic in Gold Mine Tailings, Campbell Mine, Balmertown, Ontario*. M.Sc. Thesis, University of Waterloo, Waterloo, Ontario, Canada.
- Su, C., & Puls, R. W. (2001). Arsenate and arsenite removal by zerovalent iron: Kinetics, redox

- transformation, and implications for in situ groundwater remediation. *Environmental Science and Technology*, 35(7), 1487–1492. <https://doi.org/10.1021/es001607i>
- Thamdrup, B., Finster, K., Hansen, J. W., & Bak, F. (1993). Bacterial disproportionation of elemental sulfur coupled to chemical reduction of iron or manganese. *Applied and Environmental Microbiology*, 59(1), 101–108. <http://aem.asm.org/>
- Walker, S. R., Jamieson, H. E., Lanzirrotti, A., & Andrade, C. F. (2005). The speciation of arsenic in iron oxides in mine wastes from the giant gold mine, N.W.T.: Application of synchrotron micro-XRD and micro-XANES at the grain scale. In *The Canadian Mineralogist* (Vol. 43).
- Walters, W., Hyde, E. R., Berg-Lyons, D., Ackermann, G., Humphrey, G., Parada, A., Gilbert, J. A., Jansson, J. K., Gregory Caporaso, J., Fuhrman, J. A., Apprill, A., Knight, R., & Walters, C. W. (2015). Improved bacterial 16S rRNA gene (V4 and V4-5) and fungal internal transcribed spacer marker gene primers for microbial community surveys. *MSystems*, 1(1). <https://doi.org/10.1128/mSystems.00009-15>
- Wang, A. O., Ptacek, C. J., Blowes, D. W., Gibson, B. D., Landis, R. C., Dyer, J. A., & Ma, J. (2019). Application of hardwood biochar as a reactive capping mat to stabilize mercury derived from contaminated floodplain soil and riverbank sediments. *Science of the Total Environment*, 653, 549–561. <https://doi.org/10.1016/j.scitotenv.2018.10.213>
- Waybrant, K. R., Blowes, D. W., & Ptacek, C. J. (1998). Selection of reactive mixtures for use in permeable reactive walls for treatment of mine drainage. *Environmental Science and Technology*, 32(13), 1972–1979. <https://doi.org/10.1021/es9703335>
- Waybrant, K. R., Ptacek, C. J., & Blowes, D. W. (2002). Treatment of mine drainage using permeable reactive barriers: Column experiments. *Environmental Science and Technology*, 36(6), 1349–1356. <https://doi.org/10.1021/es010751g>

Wolthers, M., Van Der Gaast, S. J., & Rickard, D. (2003). The structure of disordered mackinawite.
American Mineralogist, 88(11–12), 2007–2015. <https://doi.org/10.2138/am-2003-11-1245>

Supplemental Materials

Table 5.1 Characteristics of the reactive material.

Property	Silica Sand	Pea Gravel	Limestone	Woodchips	Leaf Compost	Zeravalent Iron
Moisture Content (%)	n/a	n/a	n/a	35.7	9.95	n/a
Bulk Density (g mL ⁻¹)	1.88	1.90	1.70	0.53	0.77	3.19

Table 5.2 Average chemical composition of influent solution ($n = 23$).

Parameter	Influent Solution
pH	3.50
Eh (mV)	424
Alk (mg L ⁻¹ as CaCO ₃)	< 1
As (mg L ⁻¹)	6.2 ^a
Mn (mg L ⁻¹)	0.66
Cl (mg L ⁻¹)	0.40
NO ₃ ⁻ (mg L ⁻¹)	2.3
SO ₄ ²⁻ (mg L ⁻¹)	214
Ca (mg L ⁻¹)	25.4
K (mg L ⁻¹)	1.5
Mg (mg L ⁻¹)	12.0
Na (mg L ⁻¹)	10.2
Si (g L ⁻¹)	22.8
Fe (mg L ⁻¹)	52.3 ^b

^a Mean concentration of As during stage II and IV

^b Mean concentration of Fe following spike of FeSO₄

Table A.3 A list of genera detected in the laboratory column samples that are known to catalyze sulfate reduction.

SRB	Mean % of total reads
<i>Desulfovibrio</i>	1.17
<i>Desulfovibrionaceae</i> *	0.57
<i>Desulfomicrobium</i>	0.52
<i>Desulfobulbaceae</i> *	0.42
<i>Desulfobulbus</i>	0.41
<i>Desulfuromonadales</i> *	0.25
<i>Desulfovibrionales</i> *	0.24
<i>Desulfobacteraceae</i> *	0.22
<i>Desulfurispora</i>	0.18
<i>Desulfatiglans</i>	0.18
<i>Desulfobacca</i>	0.17
<i>Desulfitibacter</i>	0.16
<i>Desulfomonile</i>	0.11
<i>Desulfitobacterium</i>	0.08
<i>Dethiobacter</i>	0.08
<i>Desulfoprunum</i>	0.08
<i>Desulfuromonas</i>	0.07
<i>Desulfosporosinus</i>	0.07
<i>Desulfurivibrio</i>	0.06
<i>Desulfatitalea</i>	0.05
<i>Desulfotomaculum</i>	0.04
<i>Dethiosulfatibacter</i>	0.04
<i>Desulfuromonadaceae</i> *	0.03
<i>Desulfocurvus</i>	0.03
<i>Desulfobacterales</i> *	0.02
<i>Desulfobulbaceae_ge</i>	0.02
<i>Desulfarculaceae</i> *	0.02
<i>Desulfatirhabdium</i>	0.01
<i>Desulfosarcina</i>	0.01
<i>Desulfovirga</i>	0.01
<i>Desulfomicrobiaceae</i> *	0.01
<i>Desulfocarbo</i>	<0.01
<i>Desulfuromonadales_ge</i>	<0.01

* Higher taxa that could not be identified on the genus level

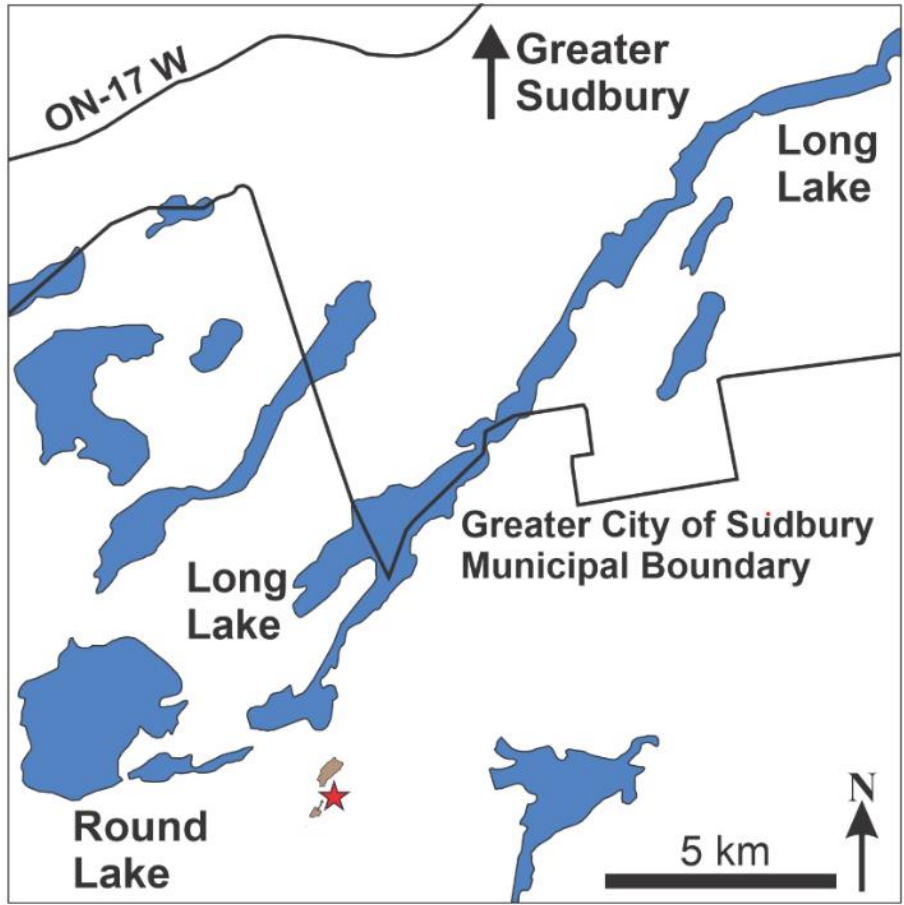


Figure 5.1 Map of Long Lake with respect to Sudbury, ON. The red star to the south of the southwest end of Long Lake is the location of the Long Lake Au Mine Tailings Impoundment (modified after Verbuyst, 2020).

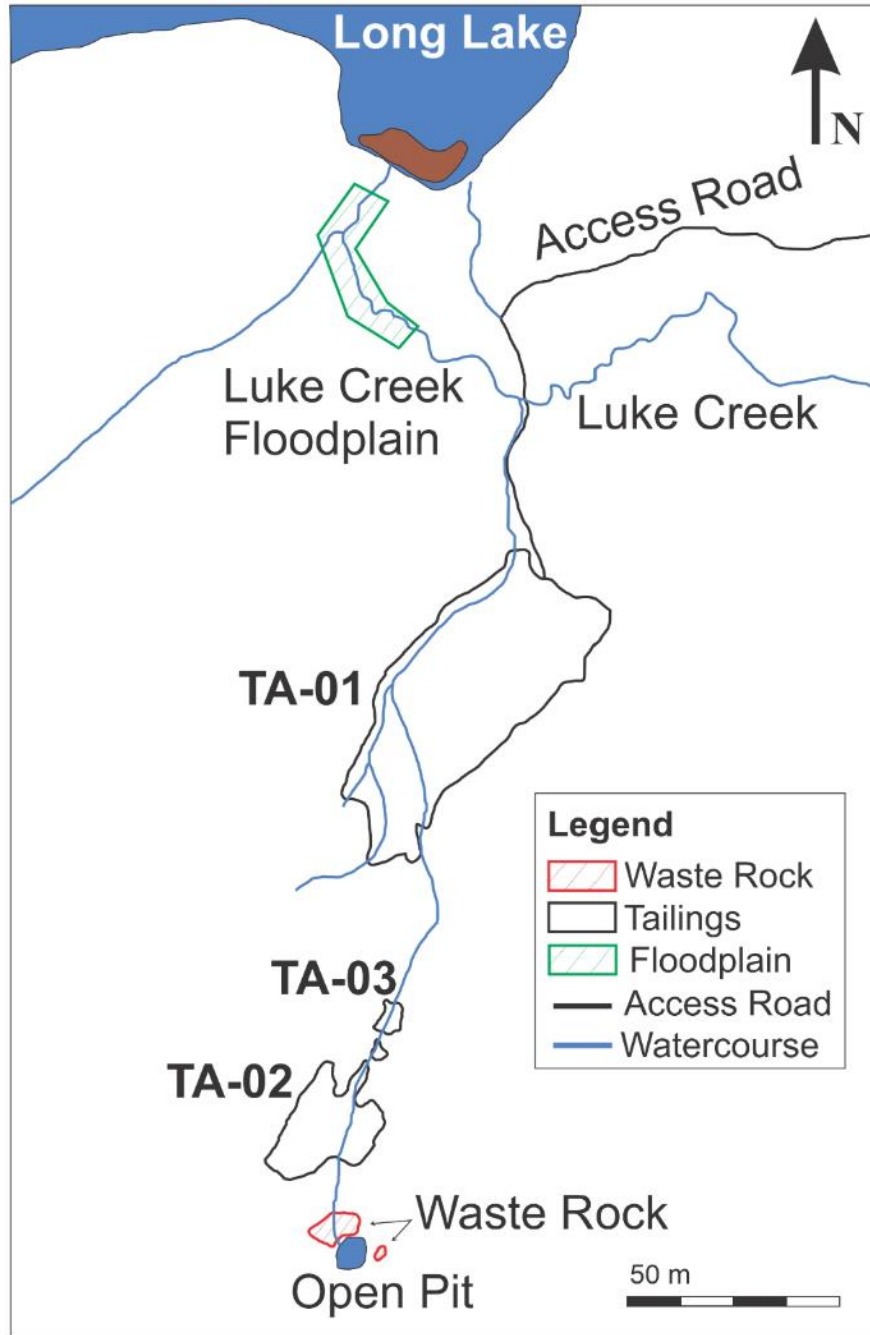


Figure 5.1 Map of the southwest end of Long Lake and tailings impoundment to the south. TA-01, TA-02, and TA-03 are the three sand-covered tailings areas (modified after Verbuyst, 2020).

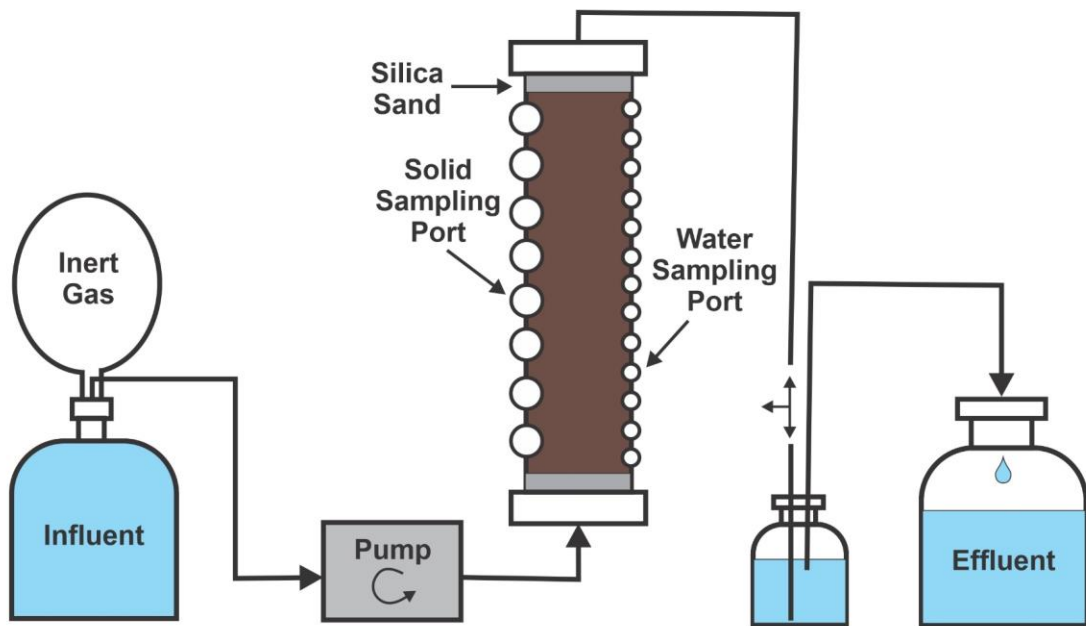


Figure 5.2 Schematic diagram of the experimental setup and column design.

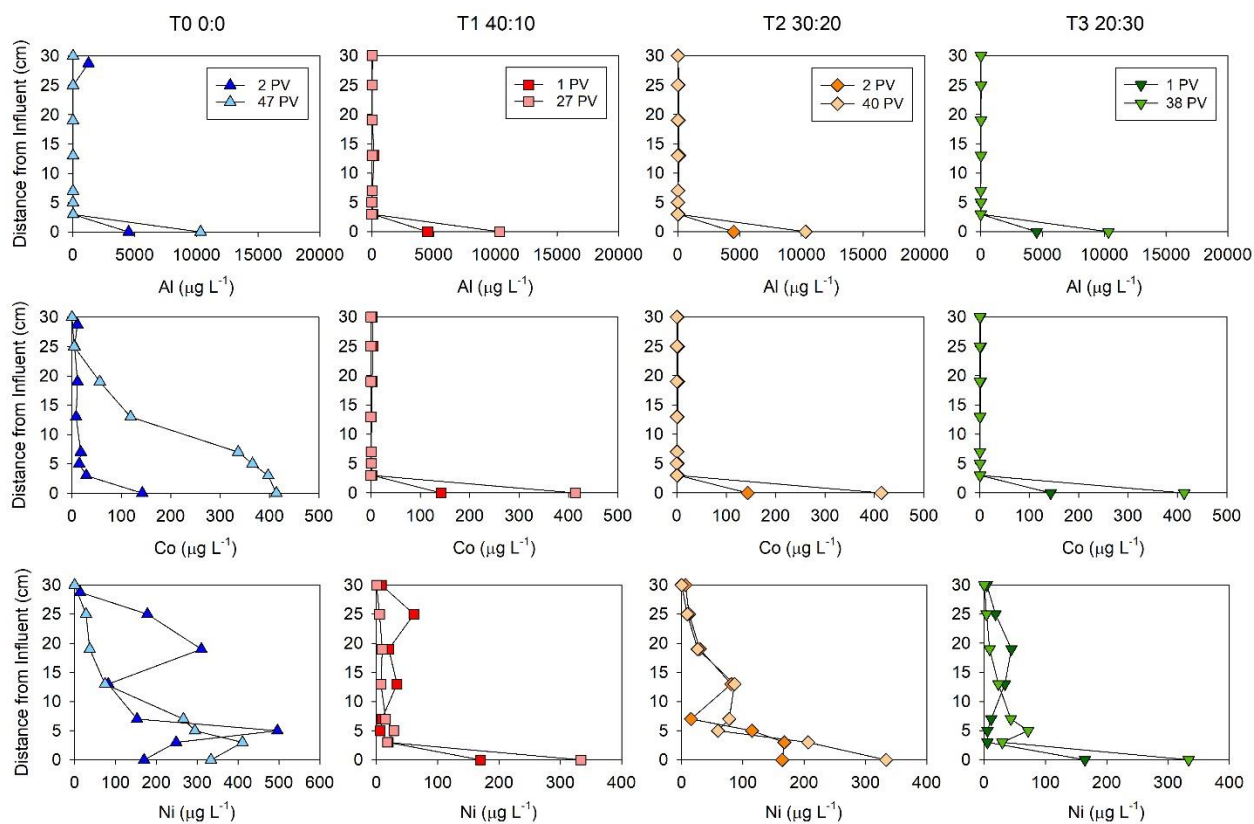


Figure 5.4 Concentrations of Al, Co, and Ni in aqueous samples collected along the length of columns T0, T1, T2, and T3 at two different time points. Each column of graphs represents a different experimental column. Distance 0 cm represents the influent concentration and 30 cm represents the effluent concentration. The OC:ZVI ratio of column T0 is 0:0, T1 is 40:10, T2 is 30:20, and T3 is 20:30.

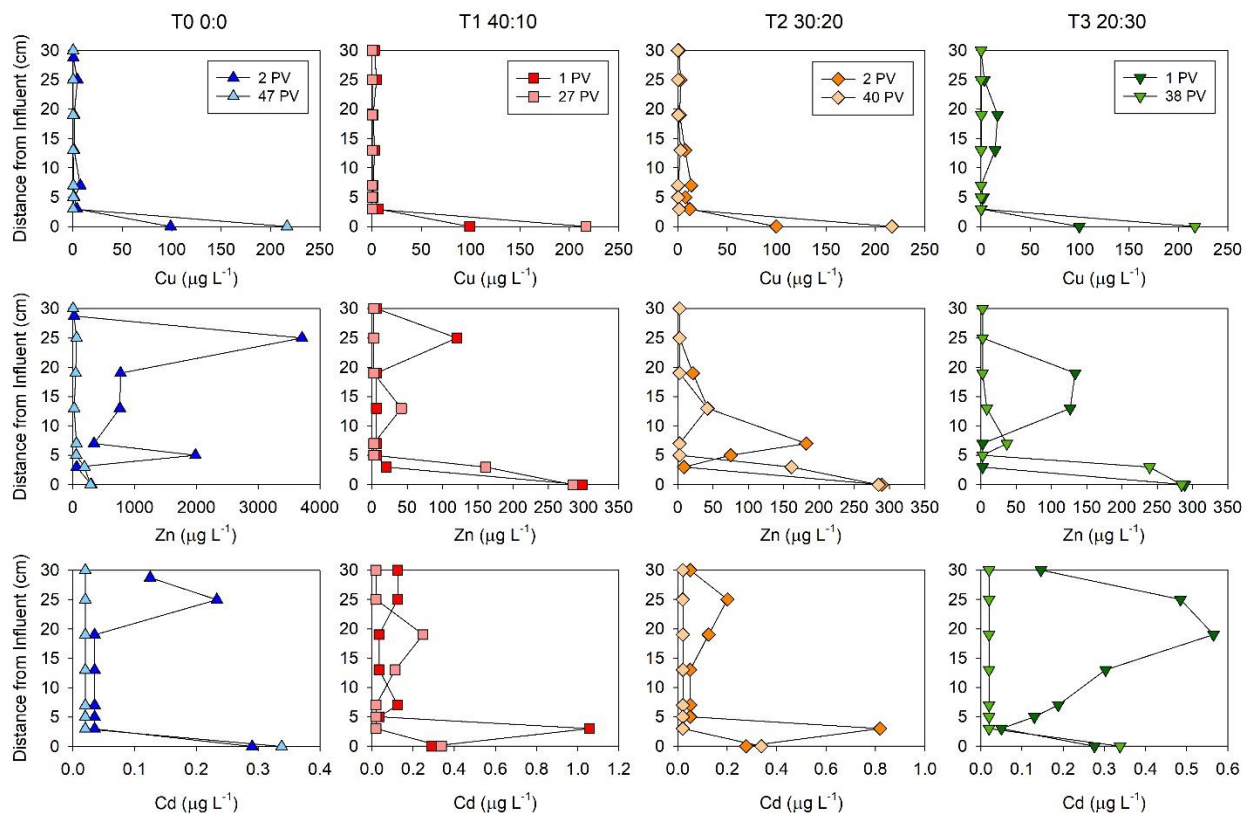


Figure 5.5 Concentrations of Cu, Zn, and Cd in aqueous samples collected along the length of columns T0, T1, T2, and T3 at two different time points. Each column of graphs represents a different experimental column. Distance 0 cm represents the influent concentration and 30 cm represents the effluent concentration. The OC:ZVI ratio of column T0 is 0:0, T1 is 40:10, T2 is 30:20, and T3 is 20:30.

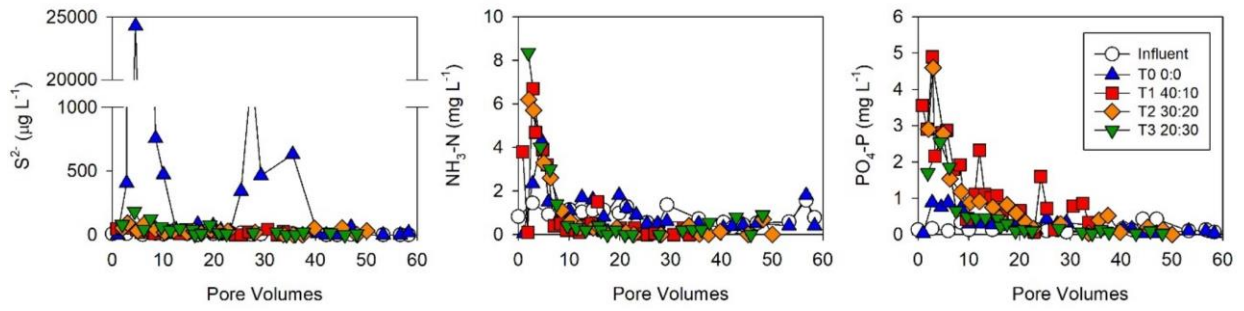


Figure 5.6 Concentrations of S^{2-} , $\text{NH}_3\text{-N}$, and $\text{PO}_4\text{-P}$ versus PVs in the influent and effluent of the four columns. The OC:ZVI ratio of column T0 is 0:0, T1 is 40:10, T2 is 30:20, and T3 is 20:30.

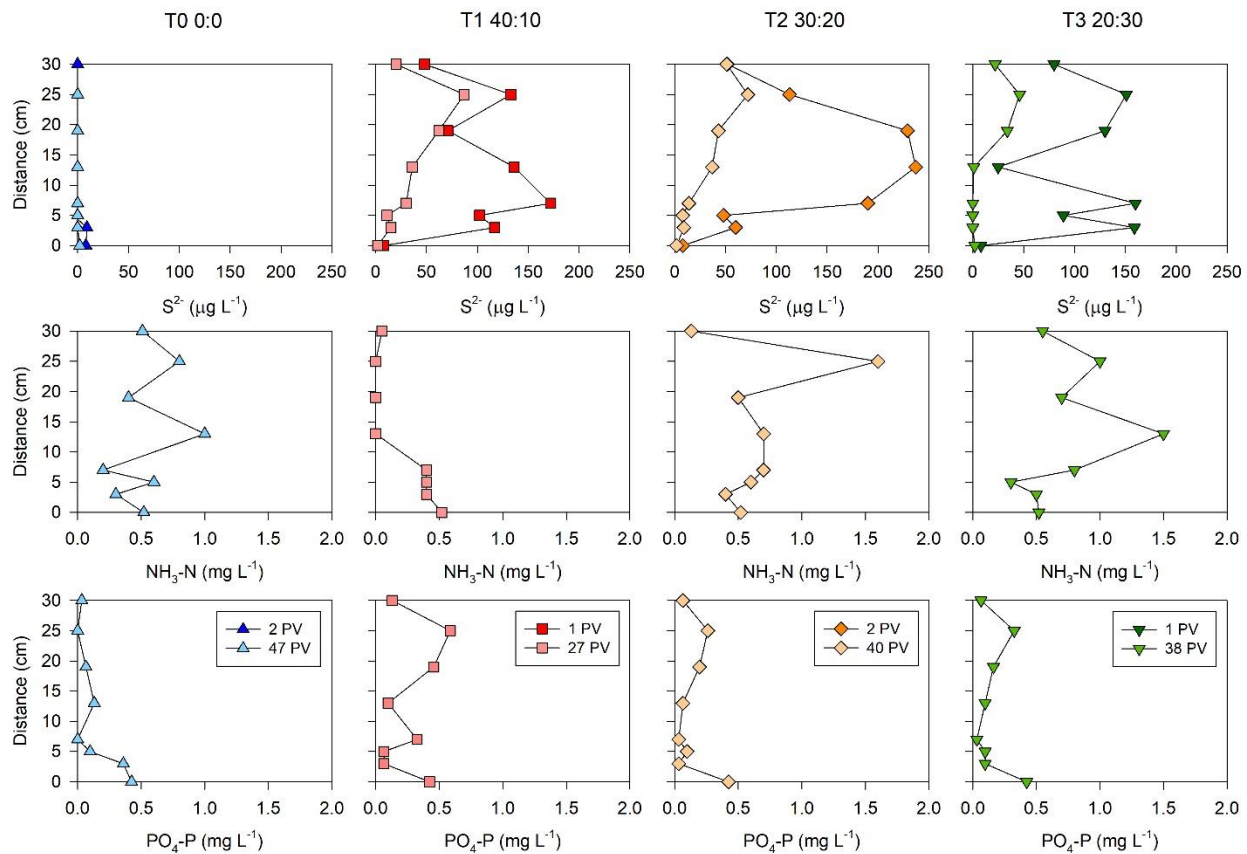


Figure 5.7 Concentrations of S²⁻, NH₃-N, and PO₄-P in aqueous samples collected along the length of columns T0, T1, T2, and T3 at two different time points. Each column of graphs represents a different experimental column. Distance 0 cm represents the influent concentration and 30 cm represents the effluent concentration. The OC:ZVI ratio of column T0 is 0:0, T1 is 40:10, T2 is 30:20, and T3 is 20:30.

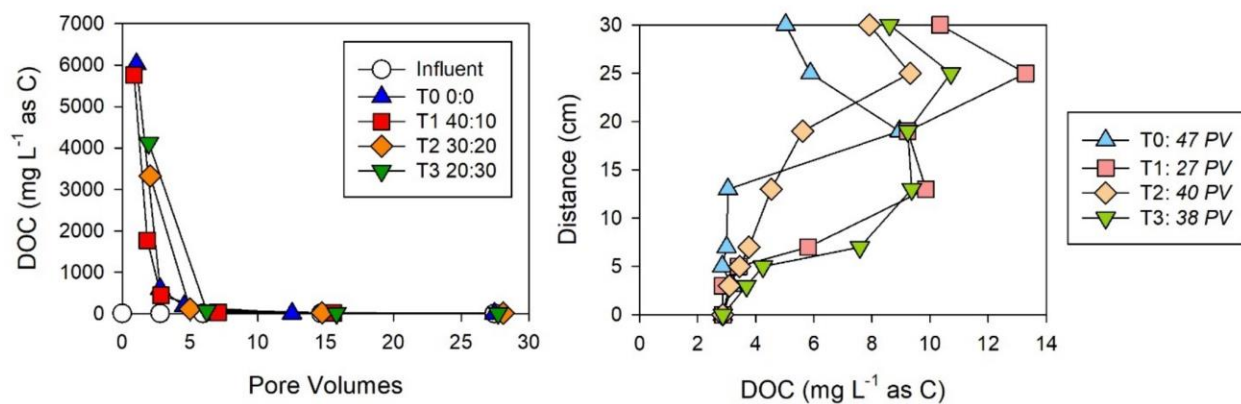


Figure A.8 Concentrations of dissolved organic carbon (DOC) versus PVs (left) compared to the changes in DOC values in aqueous samples collected along the length of columns T0, T1, T2, and T3 (right). The OC:ZVI ratio of column T0 is 0:0, T1 is 40:10, T2 is 30:20, and T3 is 20:30.

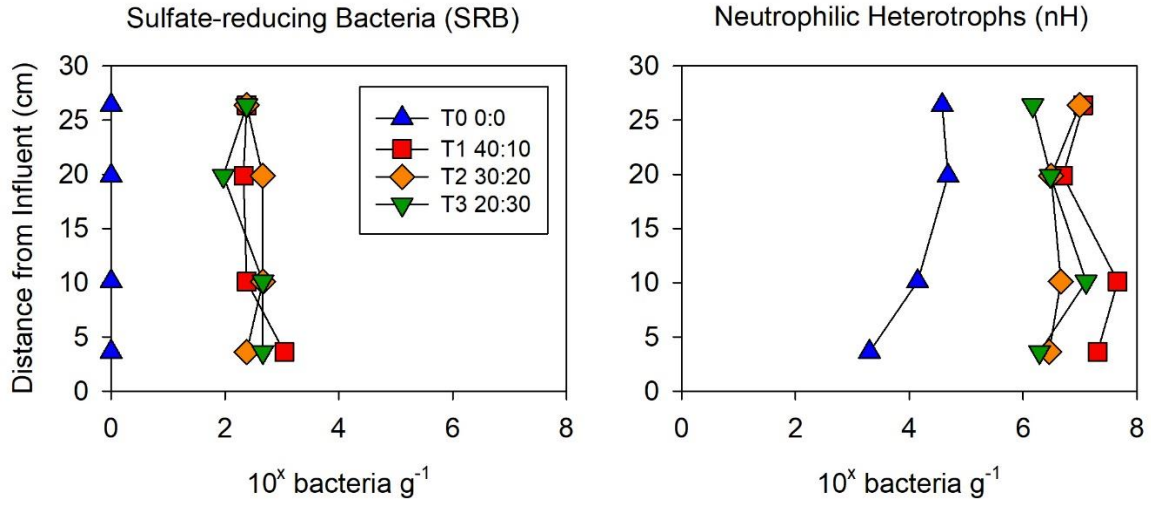


Figure A.9 MPN enumeration results for solid-phase samples collected along the length of columns T0, T1, T2, and T3. The enumeration of both sulfate-reducing bacteria (SRB) and neutrophilic heterotrophs (nH) is shown.

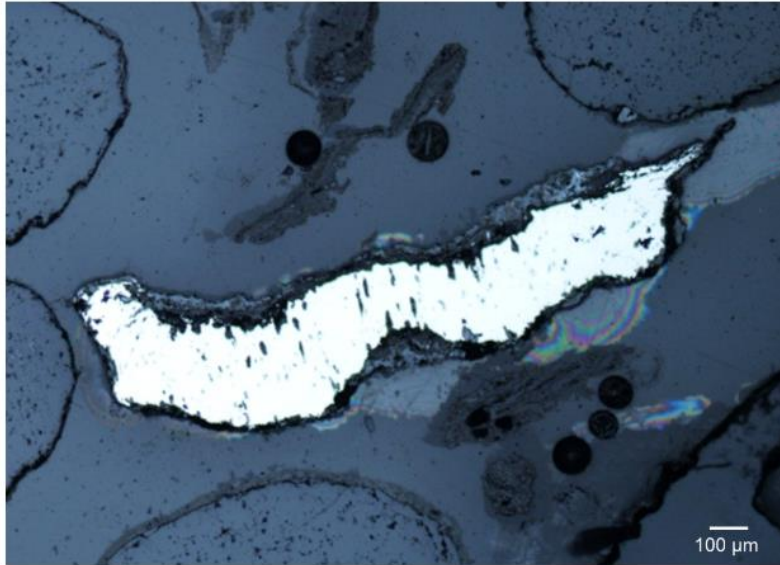


Figure 5.10 Reflected light microscopy images of a fresh zerovalent iron grain.

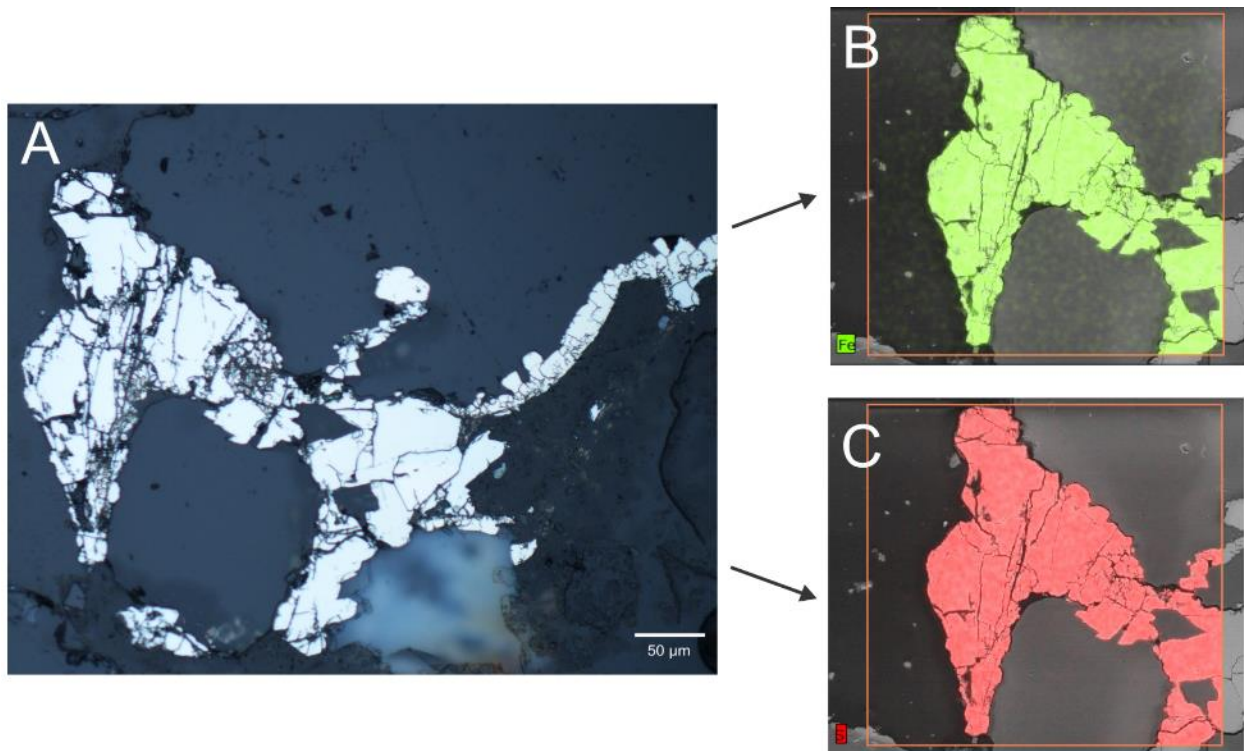


Figure 5.11 Reflected light microscopy image of the formation of a secondary precipitate around silica sand grains (A). SEM imaging of Fe- (B) and S- (C) rich precipitate (right).

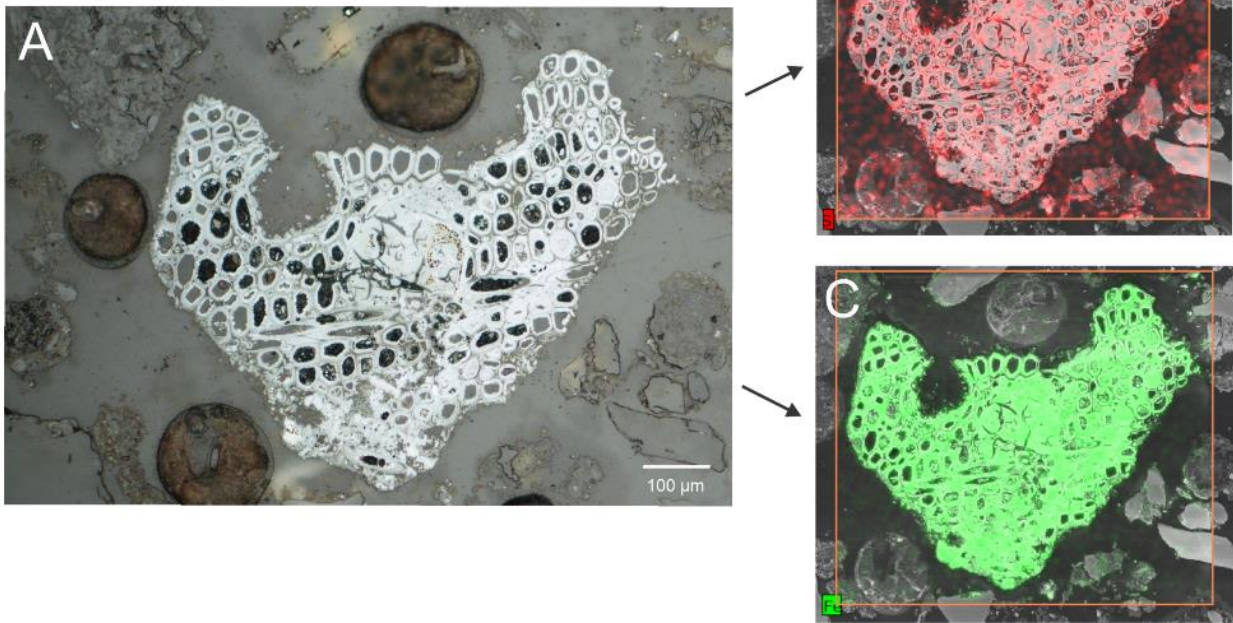


Figure A.12 Reflected light microscopy image of the replacement of OC by a secondary precipitate (A). The presence of S (B) and Fe (C) in the precipitate (right) is shown through SEM imaging.

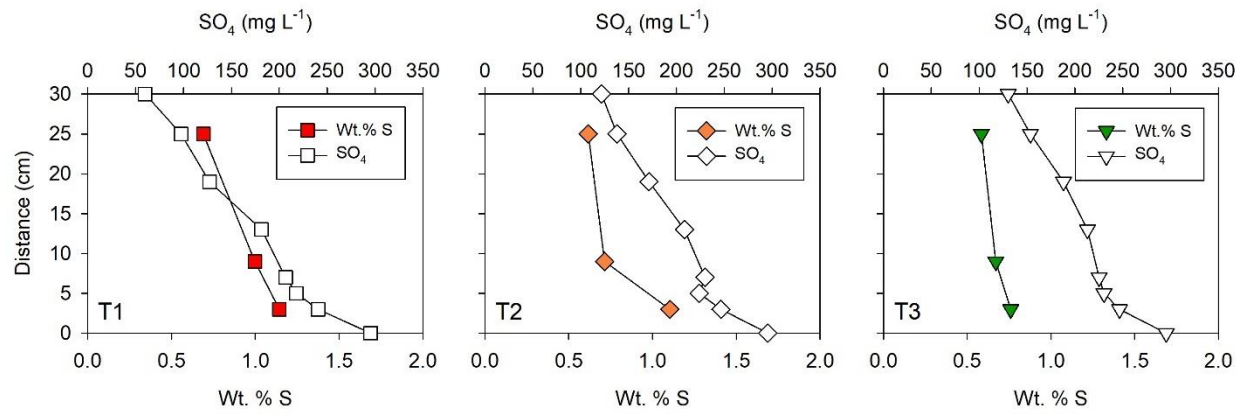


Figure 5.13 Comparison between the wt. % S in the solid column material and the aqueous SO_4^{2-} concentrations in the column porewater.

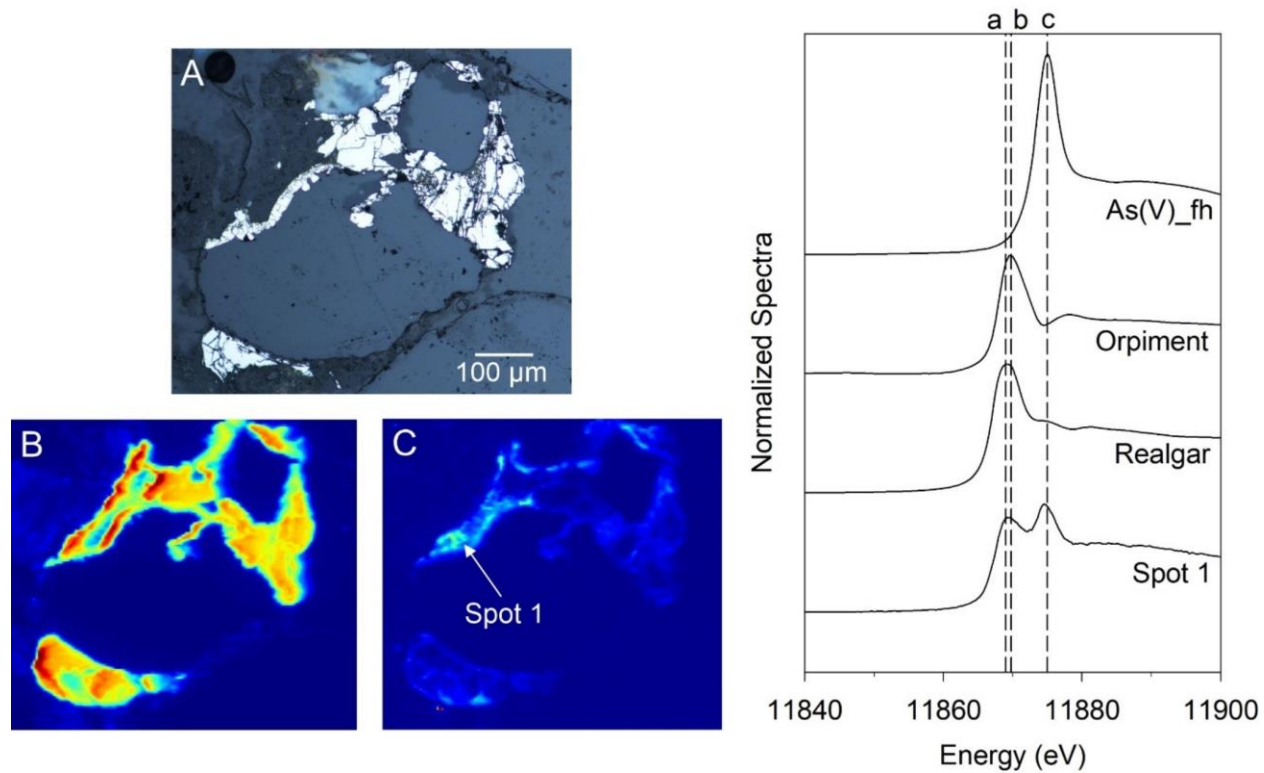


Figure A.14 Results from optical microscopy (A), Fe μ XRF imaging (B), As μ XRF imaging (C), and As μ XANES spectra (right) of a secondary precipitate that formed between grains of silica sand (column T2). The spectrum collected from spot 1 is plotted with the standards used for LCF. The spectral peak locations of realgar (a), orpiment (b), and As(V) sorbed onto ferrihydrite (c) are shown with dashed lines.

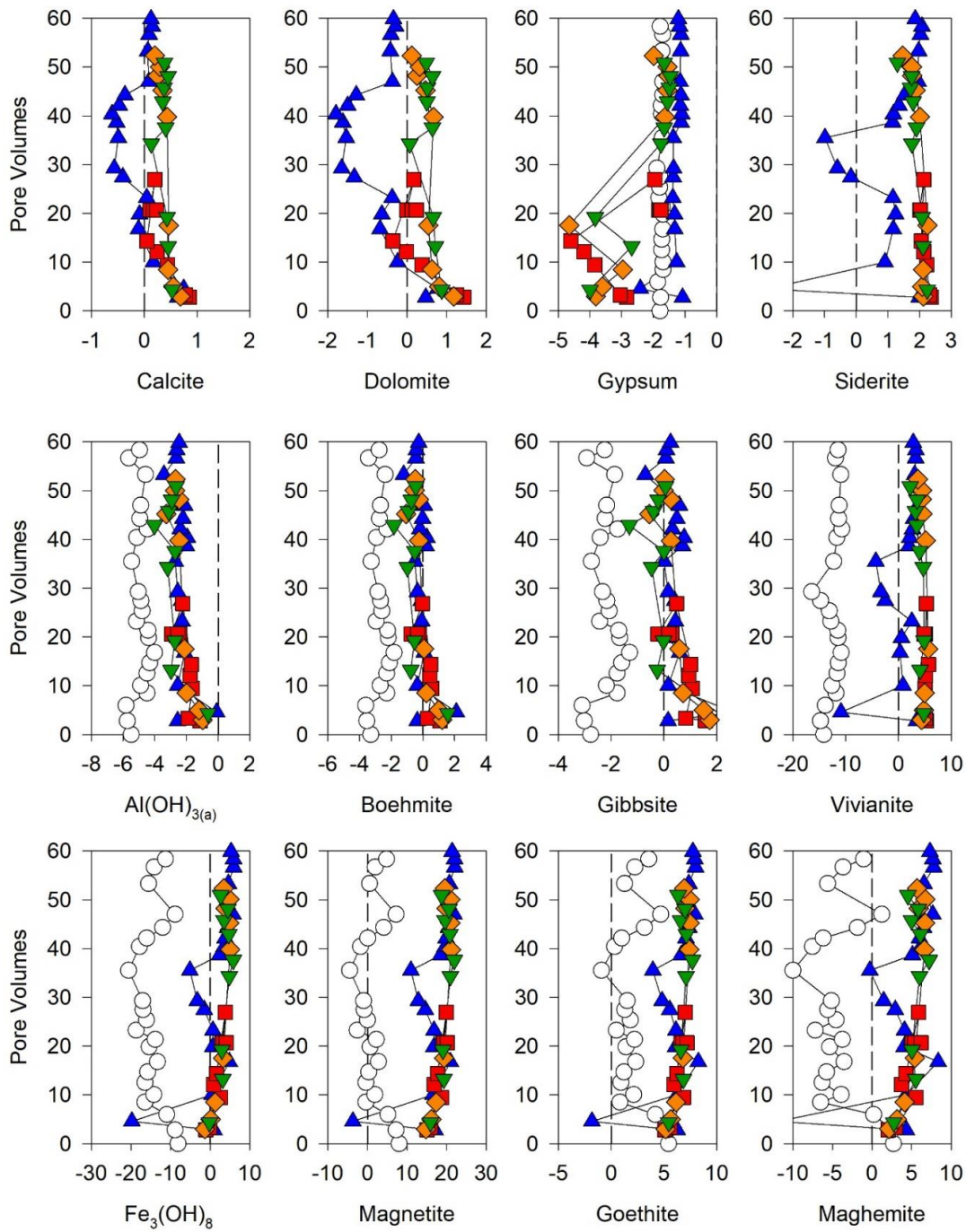


Figure 5.15 Saturation indices calculated using PHREEQCI with the WATEQ4F database for potential reaction products. The colours represent the different columns; the white circle is the influent, the blue triangle is T0, the red square is T1, the orange diamond is T2, and the green triangle is T3.

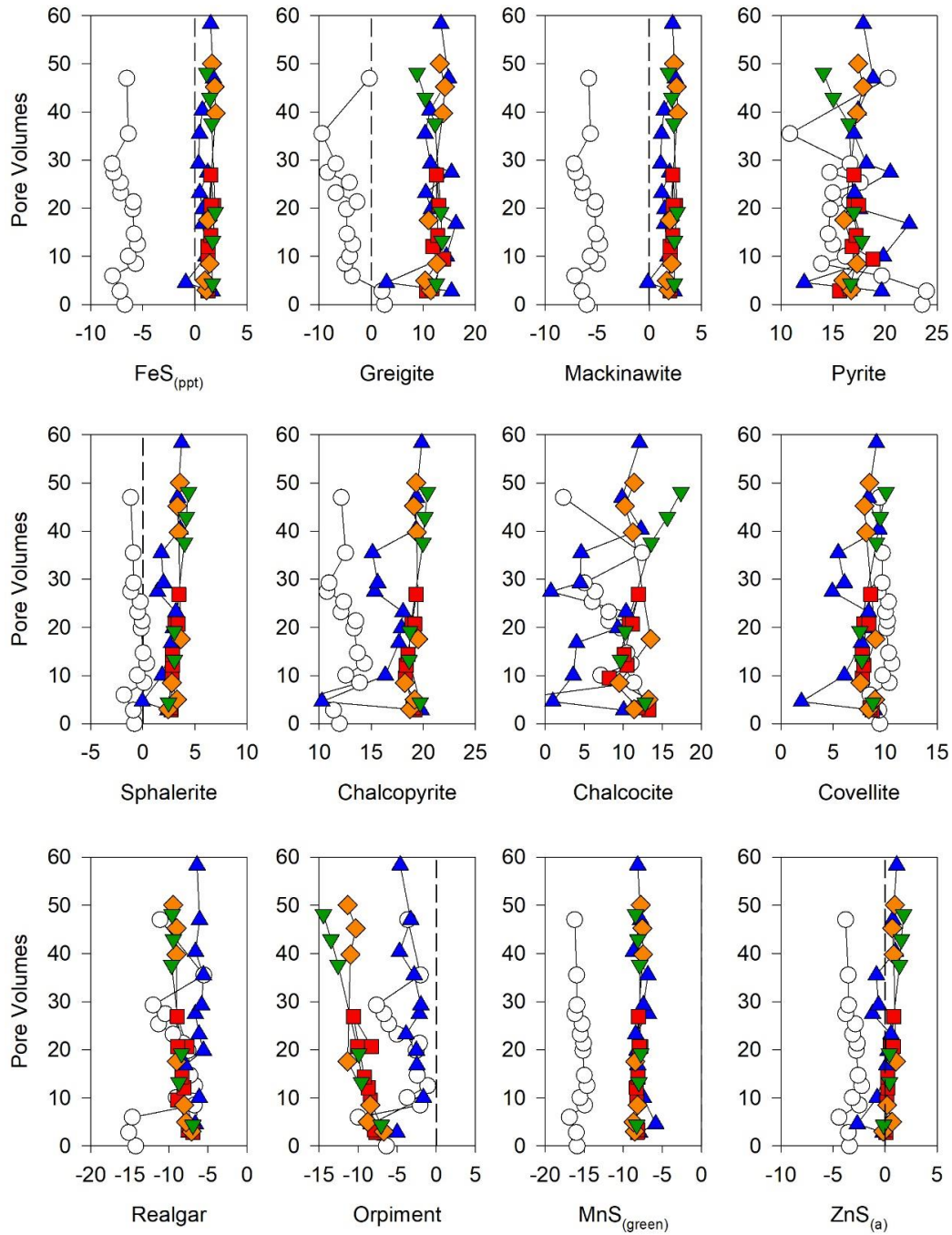


Figure 5.16 Saturation indices calculated using PHREEQCI with the WATEQ4F database for sulfide phases. The colours represent the different columns; the white circle is the influent, the blue triangle is T0, the red square is T1, the orange diamond is T2, and the green triangle is T3.

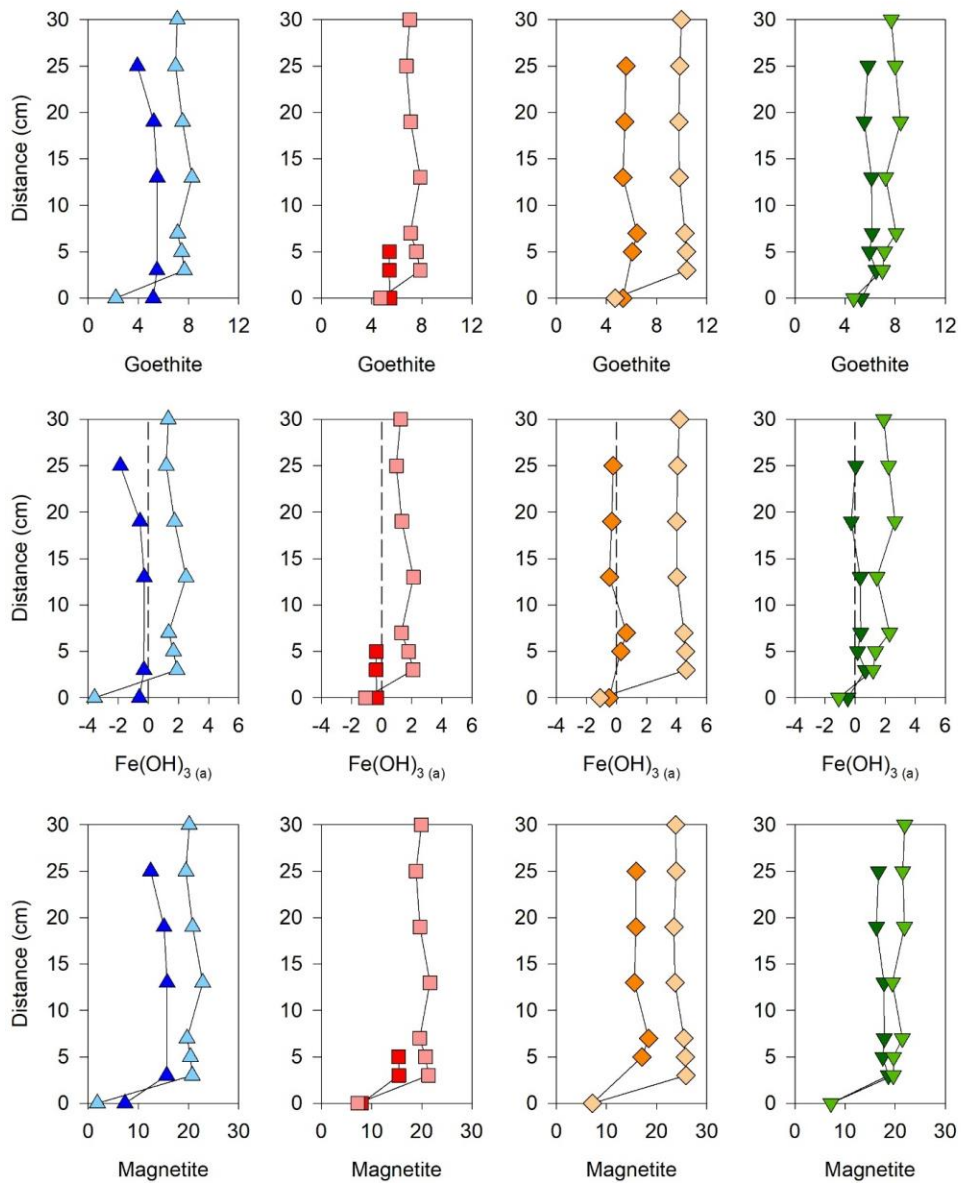


Figure 5.17 Saturation indices profiles calculated using PHREEQCI with the WATEQ4F database for goethite, Fe(OH)_3 , and magnetite. The colours represent the different columns; the white circle is the influent, the blue triangle is T0, the red square is T1, the orange square is T2, and the green triangle is T3. The darker shade of the same colour represents an earlier profile and lighter shades represent a later profile, collected towards the end of the experiment. Distance 0 cm represents the influent SI and 30 cm represents the effluent SI.

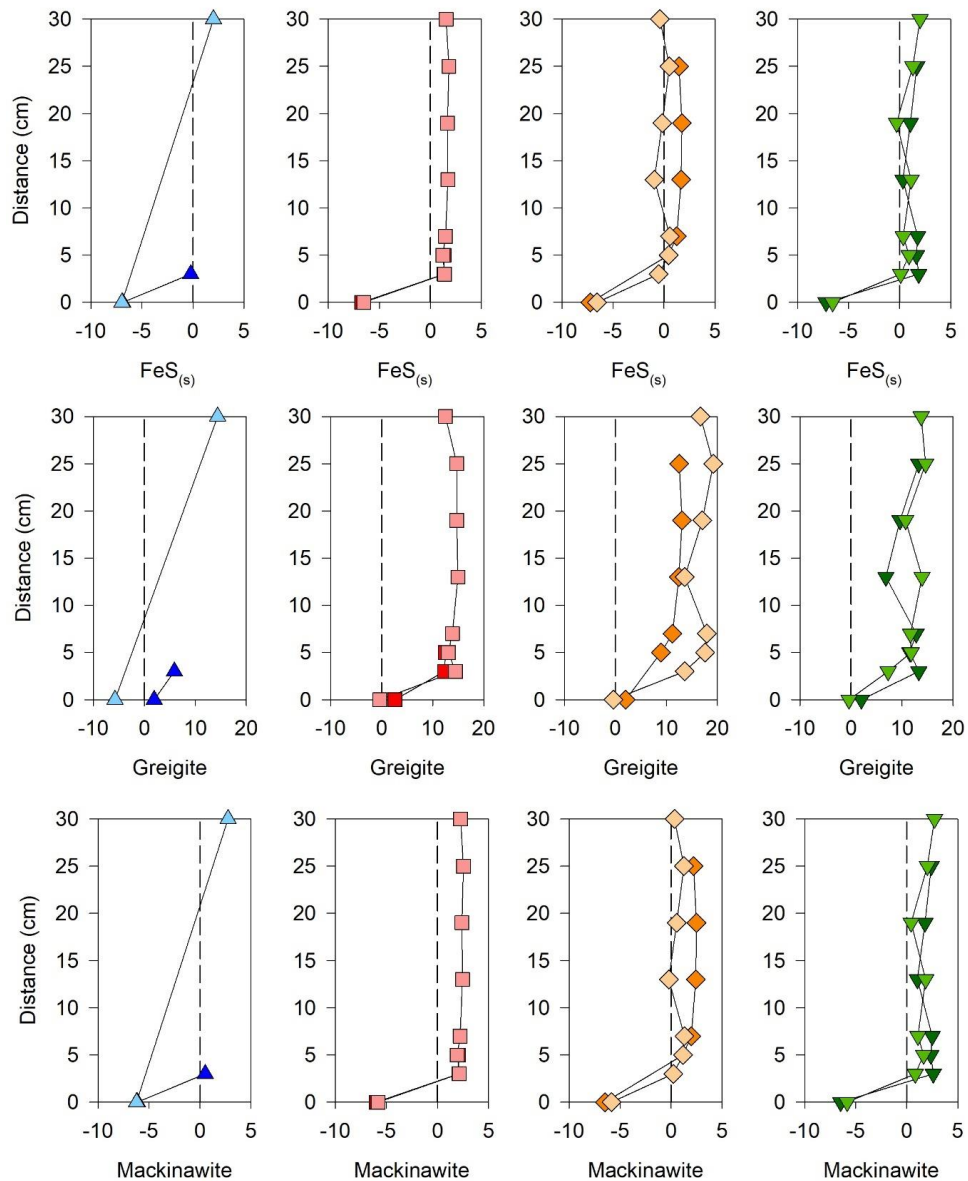


Figure 5.18 Saturation indices calculated using PHREEQCI with the WATEQ4F database for FeS_(s), greigite, and mackinawite. The colours represent the different columns; the white circle is the influent, the blue triangle is T0, the red square is T1, the orange square is T2, and the green triangle is T3. The darker shade of the same colour represents an earlier profile and lighter shades represent a later profile, collected towards the end of the experiment. Distance 0 cm represents the influent SI and 30 cm represents the effluent SI.

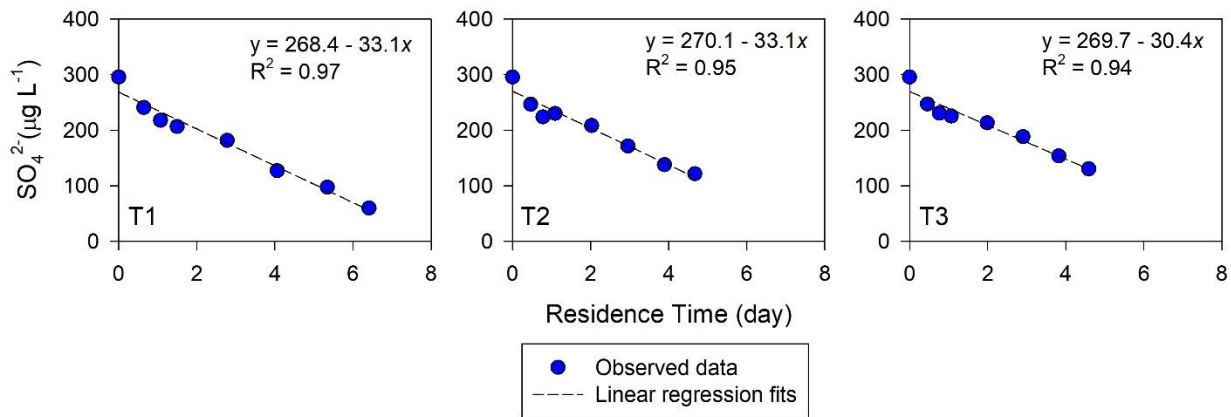


Figure A.19 Regression fits of concentration of SO_4^{2-} as a function of residence time in the three treatment columns.